Final report
IHRB Project TR-610

ON-THE-SPOT DAMAGE DETECTION METHODOLOGY FOR HIGHWAY BRIDGES

Principal Investigator
Salam Rahmatalla
Assistant Professor
Civil and Environmental Engineering
Center for Computer-Aided Design
The University of Iowa
Iowa City, IA 52242

Visiting Professor
Hee-Chang Eun
Professor
Civil and Environmental Engineering
The University of Iowa
Iowa City, IA 52242

Research Assistant
Kyle Hudson and Ye Liu
Center for Computer-Aided Design
The University of Iowa
Iowa City, Iowa 52242

Consultant
Daniel T. Ambre
Full Spectrum Diagnostics
3625 Rosewood Lane N
Plymouth, MN 55441

Sponsored by
The Iowa Highway Research Board
The Iowa Department of Transportation
Research and Technology Bureau
800 Lincoln Way, Ames, Iowa 50010

A report from
Center for Computer-Aided Design
College of Engineering
The University of Iowa
Iowa City, Iowa 52242
Phone: 319 335-5722

July, 2010

Disclaimer Notice

The contents of this report reflect the views of the authors, who are responsible for the facts and the accuracy of the information presented herein. The opinions, findings and conclusions expressed in this publication are those of the authors and not necessarily those of the sponsors.

The sponsors assume no liability for the contents or use of the information contained in this document. This report does not constitute a standard, specification, or regulation.

The sponsors do not endorse products or manufacturers. Trademarks or manufacturers' names appear in this report only because they are considered essential to the objective of the document.

The opinions, findings, and conclusions expressed in this publication are those of the author and not necessarily those of the Iowa Department of Transportation

Iowa Department of Transportation Statement of Non-Discrimination

Federal and state laws prohibit employment and/or public accommodation discrimination on the basis of age, color, creed, disability, gender identity, national origin, pregnancy, race, religion, sex, sexual orientation or veteran's status. If you believe you have been discriminated against, please contact the Iowa Civil Rights Commission at 800-457-4416 or Iowa Department of Transportation's affirmative action officer. If you need accommodations because of a disability to access the Iowa Department of Transportation's services, contact the agency's affirmative action officer at 800-262-0003.

The University of Iowa Statement of Non-Discrimination

The University of Iowa does not discriminate on the basis of race, color, age, religion, national origin, sexual orientation, gender identity, sex, marital status, disability, or status as a U.S. veteran. Inquiries can be directed to the Director of Equal Opportunity and Diversity at the University of Iowa, (319) 335-0705.

EXECUTIVE SUMMARY

Vibration-based damage identification (VBDI) techniques have been developed in part to address the problems associated with an aging civil infrastructure. To assess the potential of VBDI as it applies to highway bridges in Iowa, three applications of VBDI techniques were considered in this study: numerical simulation, laboratory structures, and field structures. VBDI techniques were found to be highly capable of locating and quantifying damage in numerical simulations. These same techniques were found to be accurate in locating various types of damage in a laboratory setting with actual structures. Although there is the potential for these techniques to quantify damage in a laboratory setting, the ability of the methods to quantify low-level damage in the laboratory is not robust. When applying these techniques to an actual bridge, it was found that some traditional applications of VBDI methods are capable of describing the global behavior of the structure but are most likely not suited for the identification of typical damage scenarios found in civil infrastructure. Measurement noise, boundary conditions, complications due to substructures and multiple material types, and transducer sensitivity make it very difficult for present VBDI techniques to identify, much less quantify, highly localized damage (such as small cracks and minor changes in thickness). However, while investigating VBDI techniques in the field, it was found that if the frequency-domain response of the structure can be generated from operating traffic load, the structural response can be animated and used to develop a holistic view of the bridge's response to various automobile loadings. By animating the response of a field bridge, concrete cracking (in the abutment and deck) was correlated with structural motion and problem frequencies (i.e., those that cause significant torsion or tension-compression at beam ends) were identified. Furthermore, a frequency-domain study of operational traffic was used to identify both common and extreme frequencies for a given structure and loading. Common traffic frequencies can be compared to problem frequencies so that cost-effective, preventative solutions (either structural or usage-based) can be developed for a wide range of IDOT bridges. Further work should (1) perfect the process of collecting high-quality operational frequency response data; (2) expand and simplify the process of correlating frequency response animations with damage; and (3) develop efficient, economical, pre-emptive solutions to common damage types.

TABLE OF CONTENTS

LIST OF FIGURES

LIST OF APPENDICES

ELECTRONIC APPENDIX (CD-ROM or IHRB FTP folder)

Video 1: MEscope animation of entire bridge ODSFRFs at 13.5 Hz (screenshot: Figure 4.37)

Video 2: MEscope animation of independent beam FRFs at 13.5 Hz (screenshot: Figure 4.38)

Video 3: MEscope North east beam 4 (NE4) boundary condition animation of ODSFRFs at 15 Hz (screenshot: Figure 4.42)

Video 4: MEscope North east beam 3 (NE3) boundary condition animation of FRFs at 151 Hz (screenshot: Figure 4.49)

Video 5: MEscope North east beam 4 (NE4) boundary condition animation of FRFs at 1 Hz (screenshot: Figure 4.50)

Video 6: MEscope North east beam 4 (NE4) boundary condition animation of FRFs at 43.5 Hz (screenshot: Figure 4.51)

Video 7: MEscope North east beam 4 (NE4) boundary condition animation of FRF's at 13.5 Hz showing significant torsional motion in exterior beam ends (screenshot: Figure 4.52)

Video 8: MEscope North east beam 3 (NE3) boundary condition animation of FRF's at 13.5 Hz showing very little torsional motion in interior beam ends (screenshot: Figure 4.53)

Technical Report Documentation Page

1. Report No. **IHRB Project TR-610**	**2. Government Accession No.**	**3. Recipient's Catalog No.**	
4. Title and Subtitle **On The Spot Damage Detection Methodology For Highway Bridges**		**5. Report Date** July 2010	
		6. Performing Organization Code	
7. Author(s) Salam Rahmatalla, Kyle Hudson, Ye Liu, Hee-Chang Eun, Daniel Ambre		**8. Performing Organization Report No.**	
9. Performing Organization Name and Address The Center for Computer-Aided Design The University of Iowa 330 South Madison, Iowa City, Iowa, 52242		**10. Work Unit No. (TRAIS)**	
		11. Contract or Grant No.	
12. Sponsoring Organization Name and Address Iowa Highway Research Board Iowa Department of Transportation 800 Lincoln Way Ames, IA 50010		**13. Type of Report and Period Covered** Final Report	
		14. Sponsoring Agency Code	
15. Supplementary Notes			

16. Abstract

To assess the potential of vibration-based damage identification (VBDI) as it applies to highway bridges in Iowa, three applications of VBDI were considered in this study: numerical simulation, laboratory structures, and field structures. VBDI techniques were found to be highly capable of locating and quantifying damage in numerical simulations. These same techniques were found to be accurate in locating various types of damage in a lab setting with actual structures but were not as accurate in quantifying damage.

When applying these techniques to an actual bridge, it was found that some traditional applications of VBDI methods are capable of describing the global behavior of the structure but are most likely not suited for the identification of typical damage scenarios found in civil infrastructure, due to measurement noise, boundary conditions, complications due to substructures and multiple material types, and transducer sensitivity.

However, while investigating VBDI techniques in the field, it was found that if the frequency-domain response of the structure can be generated from operating traffic load, the structural response can be animated and used to develop a holistic view of the bridge's response to various automobile loadings. By animating the response of a field bridge, concrete cracking (in the abutment and deck) was correlated with structural motion and problem frequencies (i.e., those that cause significant torsion or tension-compression at beam ends) were identified. Furthermore, a frequency-domain study of operational traffic was used to identify both common and extreme frequencies for a given structure and loading. This novel approach, operational response and waveform analysis (ORWA), may assist bridge engineers in their decision making regarding the maintenance plans and management.

17. Key Words Vibration-based damage detection, FRF Curvature Method, operational response		**18. Distribution Statement** No restrictions.	
19. Security Classification (of this report) None	**20. Security Classification (of this page)** None	**21. No. of Pages** 72	**22. Price** NA

Form DOT F 1700.7 (8-72) **Reproduction of completed page authorized**

1. INTRODUCTION

1.1 Motivation

Maintaining a safe and reliable civil infrastructure is of utmost importance to the national economy and well-being of all citizens. With more than half of the 600,000 bridges in the United States built before 1975, areas of research related to bridge maintenance, inspection, and monitoring have received significant attention in recent years (U.S. Department of Transportation Federal Highway Administration, 2010). In Iowa, especially, where 21% of the almost 25,000 bridges are structurally deficient and over 1,000 bridges are more than 100 years old, the development of technologies related to damage detection and extension of bridge life is crucial to the state's economic growth (U.S. Department of Transportation Federal Highway Administration, 2010). Through the use of health-monitoring systems, a deeper understanding of a given bridge's integrity beyond what visual inspection provides can be achieved. With this knowledge, designers and maintenance professionals can create a relevant and cost-effective strategy for maximizing the life of the bridge. Issues that must be addressed by a health-monitoring system generally fall into two categories: reliability and accuracy of the method and efficiency of the method when applied to an actual structure. When considering a damage detection tool's reliability and accuracy, ideally it would address all of the four damage issues in bridges: (1) detecting damage; (2) locating regions of damage; (3) quantifying the severity of damage; and (4) predicting remaining service life (Rytter, 1993). Unfortunately, due to inevitable noise in field measurements, complicated boundary conditions, difficulty of measuring large structures with multiple materials, and potentially inadequate transducer sensitivity, even the most state-of-the art damage detection methods struggle to provide insight into one or more of these issues when applied to civil infrastructure (Adewuyi, Wu, & Serker, 2009; Chang, Flatau, & S.C., 2003). When considering a system's efficiency, ideally it would be low cost, portable, applicable to various bridge sizes and types, and usable at almost any time, including natural emergencies. Complicating this issue is the fact that many types of damages in structures, especially at their earlier stages, are highly localized (Guo, Xiaozhai, Dong, & Chang, 2005), and therefore the most accurate and reliable methods for detecting these damages must also be localized, unique, and oftentimes permanent. Nevertheless, with proper use, methods such as

vibration-based damage identification (VBDI) have shown promise in their ability to supplement current inspection and design techniques.

1.2 Background

Local damage detection techniques such as acoustic approaches (i.e., ultrasonic, impact-echo, tap test), visual approaches (i.e., X-ray and Gamma ray), and standard strain gauge approaches have been proven to accurately detect damage in the region very close to where the technology is deployed (Guo, Xiaozhai, Dong, & Chang, 2005). However, the logistics and cost associated with using these methods on civil infrastructures can outweigh the benefits even for relatively small structures (Chang, Flatau, & S.C., 2003; Guo, Xiaozhai, Dong, & Chang, 2005). Global damage detection techniques such as distributed strain measurement, fiber optic measurement and dynamic testing (through VBDI) can deliver a broader view of the structure as a whole (Li & Wu, 2007). Due to the high cost of distributed strain gauges and fiber optics, VBDI has received much attention in recent years. The concept of VBDI methods is that a change in dynamic characteristics (mass, stiffness, or damping) can be detected by observing the associated change in modal parameters such as natural frequency, mode shape, and FRF.

Modal analysis methods have become powerful tools for damage detection in bridges since 1991 when Pandey et al. proposed the idea of using mode shape curvature as an indicator of the local structural flexibility. In this way, if a crack occurs in a structure, the flexibility of the structure will increase, leading to an increase in the magnitude of the curvature. Most of the methods in this category compare mode shape curvatures of healthy (undamaged) and damaged structures and therefore require accurate finite element models of the structure. Several researchers (Maia & Silva, 2003; Farrar & Jauregui, 1994) have based their algorithms on different variations of assessing the curvature of mode shapes. The main disadvantage of this class of approaches is its reliance on highly accurate solving of a modal analysis problem, which is very hard to achieve in practice due to the existence of noise and user interactions.

Alternatively, methods based on measured frequency response functions (FRF) that use only experimental vibration data to detect structural damage have become very popular. These

methods can be applied in situations where information on the undamaged structures is available (Liu, Lieven, & Escamilla-Ambrisio, 2009; Ratcilffe, Crane, & Gillespie, 2004; Maia & Silva, 2003; Sampaio & Silva, 1999). FRF methods have proven to be relatively insensitive to noise and have been tested on real structures such as the I-40 Bridge over the Rio Grande in Albuquerque, NM, by Farrar and Jauregui (Sampaio & Silva, 1999). The FRF approach does not require the identification of the modal parameters, which is a crucial step, as it is very hard in practice to accurately extract a large number of mode shapes from the measured data; additionally, the FRF methods can be based on a wide range of frequencies and therefore have a better chance to capture localized damages in real time.

Vibration-based techniques use either controlled vibration or operational vibration to excite the structure. Whereas controlled vibration experiments calculate a mode shape and FRF from a known excitation (i.e., impact hammer or shaker), operational vibration experiments simply calculate a deflection shape or a response function at a given frequency because excitation magnitudes are unknown (i.e., traffic loading on a bridge). Typically, accelerometers are used to measure the structure's response to a given excitation;, however, in recent years Global Positioning Systems (GPS) and Micro-electromechanical Systems (MEMS) have been used with varying degrees of success (Roberts, Meng, & Dodson, 2004). In any case acceleration, velocity, or displacement data in the time domain can be transformed to the frequency domain and used to calculate either a mode shape, FRF, operating deflection shape (ODS), or operating deflection shape frequency response function (ODSFRF). All four of these parameters can be used to detect damage (by implementing a damage detection code) or to determine the relative motion of one point of the structure to another (McHargue & Richardson, 1993).

1.3 Objective

The objective of this study is to apply these state-of-the-art damage detection methods, namely VBDI, to laboratory structures and an Iowa DOT bridge in an attempt to assess the potential of an experimental approach to damage detection methodology as it applies to highway bridges in Iowa. The evaluation uses FRF curvature with various curve fitting models such as the gapped-smooth-method (GSM) to detect damage. The evaluation also

considers relative motion due to impact loading and operational loading (in the form of frequency domain animations) to complement damage detection results.

2. THEORY

2.1 Mode Shape and FRF from Equation of Motion

From Newton's second law, the dynamic properties of a multiple-degree-of-freedom system can be derived. As will be shown, the mode shape, FRF, and ODSFRF are properties of the structural system only. Although the FRF and ODSFRF are dependent on the load amplitude, they are also ratios, so for a linear system the ratio will remain the same regardless of amplitude (Richardson & Formenti, 1985). The equation of motion for a multiple-degree-of-freedom system is:

$$\boldsymbol{M}\ddot{x}(t) + \boldsymbol{C}\dot{x}(t) + \boldsymbol{K}x(t) = \boldsymbol{F}(t) \tag{2.1}$$

where **M**, **C,** and **K** are mass, damping, and stiffness matrices, respectively. $x(t) = [x_1(t),\ x_2(t), \ldots\ x_N(t)]^T$ is the displacement vector with values x_n equal to the displacement at each measured point, and $f(t) = [f_1(t),\ f_2(t), \ldots\ f_N(t)]^T$ is the load or excitation vector with values f_n equal to the excitation at each point. The mode shapes for the system can be determined:

$$\varphi = [\varphi_1,\ \varphi_2, \ldots\ \varphi_N]^T = Eigenvector\{\boldsymbol{K}, \boldsymbol{M}\} \tag{2.2}$$

Assuming that the forcing function is complex, $f(t) = f\ e^{i\Omega t}$, the solution to Equation 2.1 is $x(t) = Xe^{i\Omega t}$. Substituting this solution back into Equation 2.1 gives:

$$-\Omega^2 \boldsymbol{M}\ Xe^{i\Omega t} + i\Omega\ \boldsymbol{C}\ Xe^{i\Omega t} + \boldsymbol{K}X\ e^{i\Omega t} = \boldsymbol{F}e^{i\Omega t} \tag{2.3}$$

Solving for the displacement response, Equation 2.3 becomes:

$$X = X(\Omega) = \frac{\boldsymbol{F}}{[-\Omega^2\ \boldsymbol{M}+i\ \Omega\ \boldsymbol{C}+\boldsymbol{K}]} = \boldsymbol{H} * \boldsymbol{F} \tag{2.4}$$

For the i^{th} mode coordinate and the p^{th} excitation point, modal superposition can be used to determine a particular modal stiffness, mass, damping, and force:

$$K_i = \emptyset_i^T \boldsymbol{K} \emptyset_{\boldsymbol{i}}\ \ ;\ \ M_i = \emptyset_i^T \boldsymbol{M} \emptyset_{\boldsymbol{i}}\ \ ;\ \ C_i = \emptyset_i^T \boldsymbol{C} \emptyset_{\boldsymbol{i}}\ ;\ \ F_i = \emptyset_i^T \boldsymbol{F}(\Omega) = \emptyset_{pr} f_p(\Omega) \tag{2.5}$$

So from Equations 2.4 and 2.5, the modal displacement response for a particular mode coordinate and excitation point is:

$$X_i(\Omega) = \frac{\emptyset_{pr} f_p(\Omega)}{[-\Omega^2\ M_i+i\ \Omega\ C_i+K_i]} = H_i * f_p(\Omega) \tag{2.6}$$

Once again, from modal superposition, the actual displacement response of the measured point *l* is:

$$x_l(\Omega) = \sum_{i=1}^{N} \emptyset_{lr}\ X_i(\Omega) \tag{2.7}$$

So from Equations 2.6 and 2.7, the actual displacement response is:

$$x_l(\Omega) = \sum_{i=1}^{N} \frac{\emptyset_{lr}\emptyset_{pr} f_p(\Omega)}{[-\Omega^2\ M_i + i\ \Omega\ C_i + K_i]} \tag{2.8}$$

From Equations 2.6 and 2.8, the FRF (with respect to displacement) between the measured point *l* and the excitation point *p* is:

$$H_{lp} = \frac{x_l(\Omega)}{f_p(\Omega)} = \sum_{i=1}^{N} \frac{\emptyset_{lr}\emptyset_{pr}}{[-\Omega^2\ M_i + i\ \Omega\ C_i + K_i]} \tag{2.9}$$

Factoring and letting $\frac{M_i}{K_i} = \frac{1}{\omega^2}$, and from $= \frac{c}{2m\omega} \rightarrow \frac{C_i}{K_i} = \frac{2\,\xi}{\omega}$, Equation 2.9 becomes:

$$H_{lp} = \sum_{i=1}^{N} \frac{\emptyset_{lr}\emptyset_{pr}}{K_i[-(\Omega/\omega)^2\ 2\ i\ \omega\ \xi\ (\Omega/\omega)+1]} \tag{2.10}$$

Finally, the FRF with respect to acceleration is $H_{lp,acc} = -\omega^2 H_{lp,displ}$ so:

$$H_{lp,acc} = \sum_{i=1}^{N} \frac{-\omega^2\emptyset_{lr}\emptyset_{pr}}{K_i[-(\Omega/\omega)^2\ 2\ i\ \omega\ \xi\ (\Omega/\omega)+1]} \tag{2.11}$$

2.2 FRF and ODSFRF from Spectral Measurements

Equation 2.11 is the analytical definition of FRF, but for experimental purposes it is easier to view the FRF as a function of the cross and auto spectra, which can readily be obtained from most multi-channel data acquisition systems. The cross spectrum is computed by multiplying the Fourier spectrum of a measured response by the complex conjugate of the Fourier spectrum of a known input:

$$G_{xy}(\omega) = F_x(\omega)F_y^*(\omega) \tag{2.12}$$

The auto spectrum is computed by multiplying the Fourier spectrum of the input by the complex conjugate of itself.

$$G_{yy}(\omega) = F_y(\omega)F_y^*(\omega) \tag{2.12}$$

The FRF is then defined as the ratio of the cross and auto spectrum:

$$FRF(\omega) \equiv \alpha = G_{xy}(\omega)/G_{yy}(\omega) \tag{2.13}$$

Obviously, the FRF is a dynamic property that can be calculated only if the excitation is a known quantity. However, in many experimental applications, it is much easier to use ambient or operational vibration to excite the structure as opposed to applying a known load. In these situations, as in the case with using traffic loading as vibration for damage detection on a bridge, a different kind of dynamic characteristic must be calculated. Vibrant Technologies has developed the ODSFRF, which is calculated by replacing the magnitude of the cross spectrum with the square root of the magnitude of the response auto spectrum (Schwarz & Richardson, 2004).

$$ODSFRF(\omega) \equiv \beta = \sqrt{G_{xx}}\frac{G_{xy}(\omega)}{|G_{xy}(\omega)|} = \overline{F_x(\omega)} \tag{2.14}$$

2.3 Mode Shape Curvature Method

The mode shape curvature method was proposed based on the premise that for a given moment applied to a structure, a reduction in stiffness associated with damage will cause an increase in the curvature of the mode shape (Pandey, Biswas, & Samman, 1991). The mode shape curvature of the structure is typically computed using numerical differentiation of shapes at evenly spaced intervals:

$$\varphi_i'' = \frac{\varphi_{i+1} - 2\varphi_i + \varphi_{i-1}}{h^2} \tag{2.15}$$

A damage index can be computed by summing the absolute difference or absolute squared difference of the damaged and baseline mode shapes for all impact points:

$$\Delta\varphi_i'' = \sum_j \left| \varphi''^2_{ij} - \varphi''^{*2}_{ij} \right| \tag{2.16}$$

The disadvantage of the mode shape curvature method is that the mode shapes have to be accurately solved to produce accurate results. For large systems, this task is difficult and can be expensive to implement. Also, relatively small noise levels can significantly distort the modal solution and are only magnified by numerical differentiation (Adewuyi, Wu, & Serker, 2009).

2.4 FRF Curvature Method

This method simply extends the mode shape curvature method proposed by Pandey et al. to all frequencies in the measurement range.

$$\alpha''_{i,j,\omega} = \frac{\alpha_{i+1,j} - 2\alpha_{i,j} + \alpha_{i-1,j}}{h^2} \tag{2.17}$$

Similarly, a damage index can be computed by summing the absolute difference or absolute squared difference of the damaged and baseline FRFs for all impact points:

$$\Delta\alpha''_{i,\omega} = \sum_j \left| \alpha''^2_{ij} - \alpha''^{*2}_{ij} \right| \tag{2.18}$$

A second damage index can be computed by summing Equation 2.18 for all frequencies in the measurement range:

$$S_i = \sum_\omega \Delta\alpha''_{i,j} \tag{2.19}$$

The FRF curvature method's main advantage is that there is no need to perform a modal analysis. The FRF can be readily obtained from standard data acquisition software.

2.4.1 Numerical Simulation with FRF Curvature Method

To show the FRF curvature method's ability to detect damage, a numerical simulation was completed with a 30 element long plate. The plate was assumed to have free-free boundary conditions at its ends. Two damage locations were simulated at elements 5 and 21 by decreasing the plate's thickness by 60% and 5%, respectively. Figure 2.1 shows a schematic of the plate.

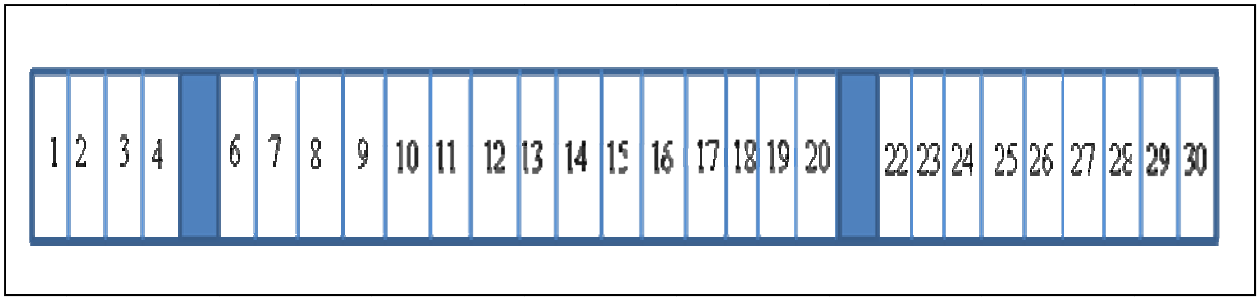

Figure 2.1 Schematic of the plate used in numerical simulation

Figures 2.2 and 2.3 show the summed damage indices for the plate using local and global curve fitting, respectively. Local curve fitting accurately locates the damage and seems to quantify the magnitudes of the damage as well. Global curve fitting also locates the damage, but fails to show a significant difference in the thickness between elements 5 and 21.

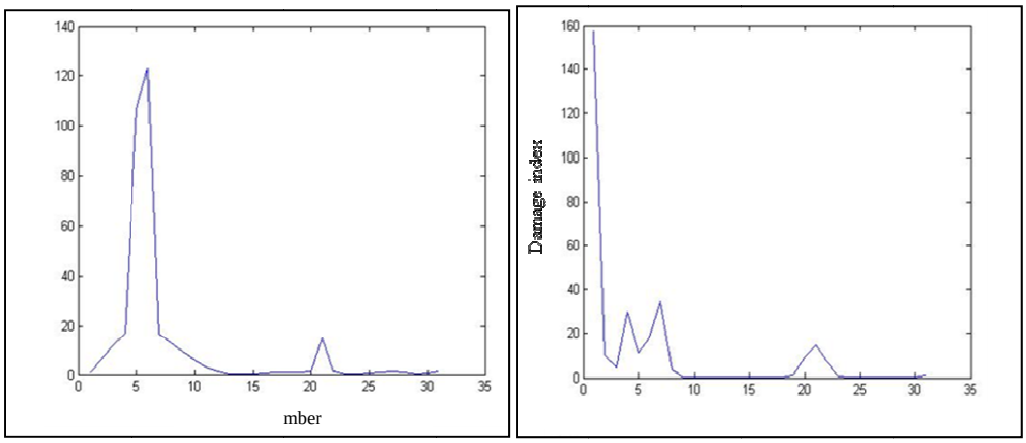

Figure 2.2 Summed Damage Index for plate using local curve fitting and Figure 2.3 Summed Damage Index for plate using global curve fitting

Because there is significant and inevitable noise in experimental measurements, the same numerical simulation was run with the addition of 1% random noise. Figures 2.4 and 2.5 show the summed damage indices for the plate with 1% noise using local and global curve fitting, respectively. Both fitting methods identify a broad damage location between elements 3 and 15 and are unable to identify any curvature change around element 21. Therefore, the addition of noise has significantly impacted the quality of the damage detection results.

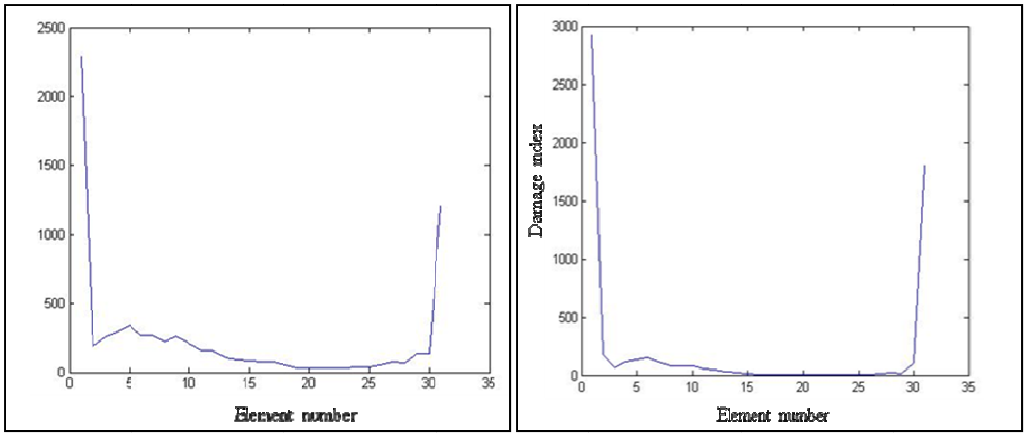

Figure 2.4 Summed Damage Index for plate with 1% noise using local curve fitting and Figure 2.5 Summed Damage Index for plate with 1% noise using global curve fitting

2.5 ODSFRF Curvature Method

Although the ODSFRF is calculated from data that is dependent only on response, the damage detection algorithm is the exact same as the FRF (Equations 2.17-2.19 apply to the ODSFRF as well). Theoretically, there is no advantage to collecting data via the ODSFRF versus the FRF because it is assumed that there will be less noise introduced in a known excitation than an operating excitation (Schwarz & Richardson, 2004). The advantage of the method is the practicality and relative ease of collecting data on civil infrastructures when no impact hammer or shaker is required.

2.6 Curve Fitting Methods

As shown in Equations 2.16 and 2.18, the mode shape curvature, FRF, and ODSFRF methods all rely on a baseline modal parameter. Unfortunately, in many circumstances, it is not possible to acquire data for an undamaged structure. Various researchers have shown that when the structure is relatively simple, it may be feasible to create a finite element model to determine the baseline mode shape or FRF (Adewuyi, Wu, & Serker, 2009; Sampaio & Silva, 1999; Ratcliffe, 2009; Maia & Silva, 2003). However, for larger structures such as bridges, it is very difficult to capture all the details that affect dynamic properties in a finite element model. In addition to time-dependent variables such as testing temperature and noise level, boundary conditions in bridges are often in between the theoretical pin, roller, and free conditions commonly used in finite element models (Ratcliffe, 2009). One

alternative to FEA and physically testing a baseline structure is curve fitting experimental data from a damaged structure, assuming that the baseline structure would yield smooth experimental data.

2.6.1 Global Curve Fitting

Global curve fitting processes all measurements together to determine the frequency and damping parameters and then uses those known values to calculate complex residues for each measurement (Richardson & Formenti, 1985). Examples of global curve fitting methods include polynomials, exponential functions, the peak (Gaussian) model, and the Fourier/power series, all of which are available in the MATLAB Curve Fitting Toolbox. MEscope software is also capable of globally smoothing FRF data, based on various fitting parameters.

2.6.2 Local Curve Fitting

In local curve fitting, each measurement is individually fit so any given curve's parameters (i.e., frequency, damping, and complex residue) are independent of another. An example of a local curve fitting method is the gapped-smoothing method (GSM), created by Ratcliffe et al. This method fits a gapped cubic polynomial to each measurement when calculating curvature, meaning that for the position x_i along the structure, the corresponding curvature is:

$$p_0 + p_1 x_i + p_1 x_i^2 + p_3 x_i^3 \tag{2.20}$$

The coefficients p_0, p_1, p_2 and p_3 are determined using C_{i-2}, C_{i-1}, C_{i+1} and C_{i+2} (curvature element C_i is gapped or left out of the calculation).

3. LABORATORY EXPERIMENTS

3.1 Equipment

Because VBDI techniques require that the dynamic characteristics of the structure be determined and analyzed, certain equipment is needed to utilize these methods. In the laboratory, a 500 lbF range Dytran impulse hammer was used to excite various structures. Six 100 g range Dytran uniaxial accelerometers were used both in the field and in the laboratory. Typically, accelerometers were fixed to structures with a magnet, but in some cases glue and wax were used. An IOtech ZonicBook/618E Data Analyzer was used to acquire data and construct FRFs. MEscope software was used to calculate mode shapes and ODSFRFs, as well as to animate data. MATLAB was used to implement VBDI algorithms. Figure 3.1 shows a typical laboratory forced vibration test setup.

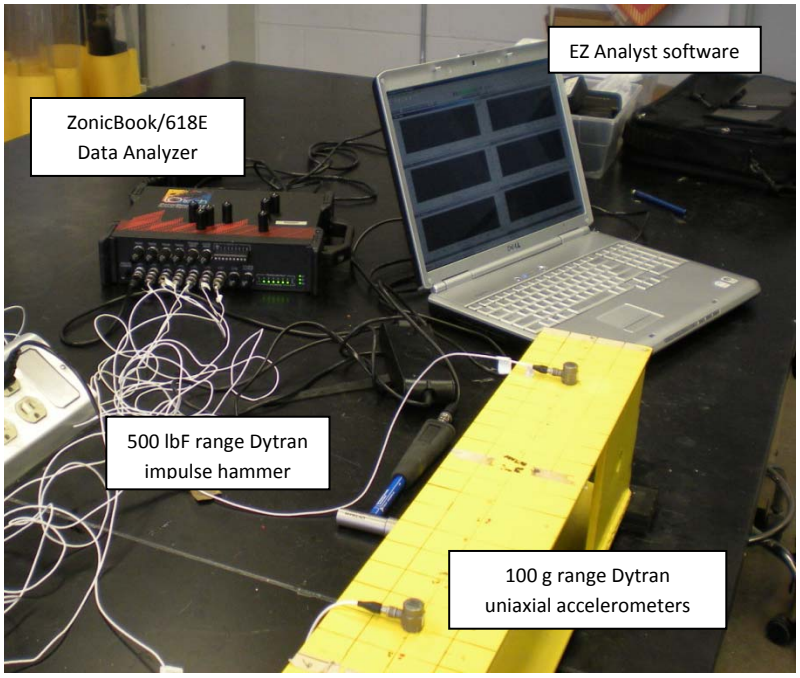

Figure 3.1 Typical VBDI test setup

3.2 I-beam

Laboratory testing was completed on a W6x9 beam 81 inches in length and simply supported by hard rubber pads at its ends. Both baseline and damaged forced excitation tests were run

on the I-beam. Damage was simulated by fixing masses of different sizes to the centerline of the top flange of the beam, thereby creating a local change in mass and stiffness in the region surrounding each mass. Figure 3.2 shows a cross section of the I-beam. Two different methods were used to determine the dynamic response of the I-beam due to forced excitation: roving response and roving excitation. For both methods, frequencies from 0-10000 Hz were analyzed with a spectral density of 1 line/6.25 Hz.

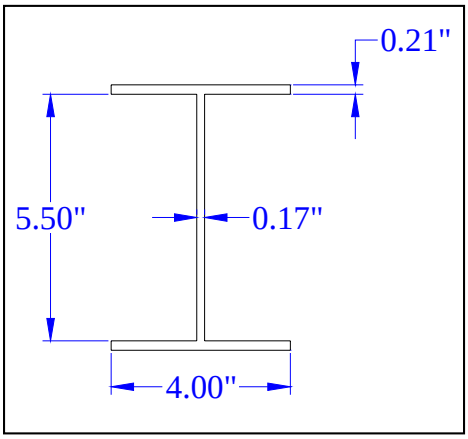

Figure 3.2 Cross section of 81" long laboratory I-beam

3.2.1 Forced Vibration Test with Two Centerline Damage Locations

During a roving excitation test, the I-beam was impacted at each node and six accelerometers were fixed to various nodes on the structure. Figure 3.3 shows a picture of a typical roving excitation setup. As shown in Figure 3.4, accelerometers were fixed on nodes 4, 16, 26, 43, 55, and 74. Similarly to the roving response test setup, for damaged beam tests, a mass of 1.7 kg was fixed to the top flange between nodes 60 and 62, and a mass of 0.5 kg was fixed to the top flange between nodes 33 and 36.

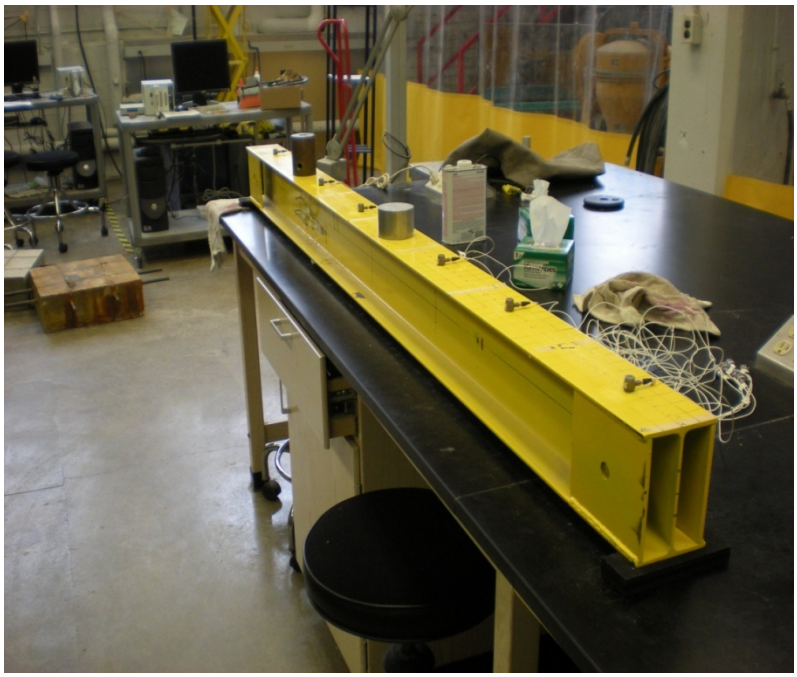

Figure 3.3 Typical laboratory I-beam setup with six fixed accelerometers and two damage zones

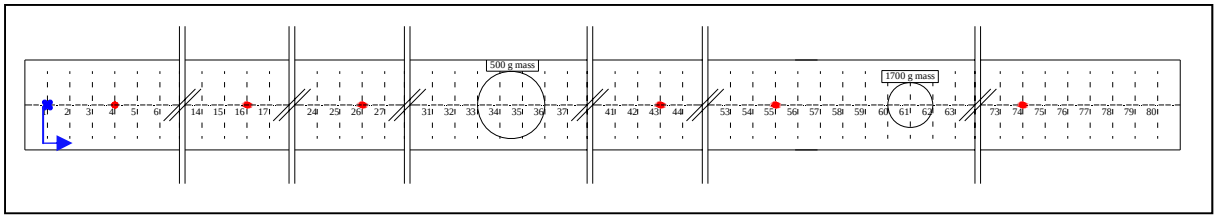

Figure 3.4 Roving excitation test setup with two damage zones

Various excitation meshes were considered during testing to determine the sensitivity of the damage detection algorithms to mesh size. The most common test ran was one impact per inch, but one impact per 2 inches, 4 inches, and 6 inches were also run. For each excitation point, the beam was impacted five times, creating 30 FRFs (one FRF for each fixed response per excitation). These FRFs were then averaged for each impact point. Therefore, with 80 excitation points and six fixed responses, 480 FRFs were created. Assuming that each accelerometer is able to capture the dynamic characteristics of the entire structure (i.e., the accelerometer is not located on a stationary modal coordinate and sensitivity is not an issue), these 480 FRFs can be averaged for each accelerometer, creating 80 usable FRFs.

3.2.1.1 Identification of two masses

Figure 3.5 shows all 480 overlaid FRFs from 0-2000 Hz collected from a roving excitation test (see Section 3.2.2) on the undamaged I-beam. Although these FRFs are not needed in the damage detection algorithms, they can be compared to the FRFs from the same structure with added damage. Figure 3.6 shows the overlaid FRFs from 0-2000 Hz collected from a roving excitation test on the I-beam with two masses fixed to the top flange. The small mass between nodes 33 and 36 and the large mass between nodes 60 and 62 represent 1.8% and 6% of the beam's total mass, respectively. In comparing Figures 3.5 and 3.6, one can notice both a change in shape of the FRFs and a shift in natural frequencies. Although observation of a shift in natural frequencies identifies the presence of damage, other methods must be used to locate and quantify the damage (i.e., VBDI algorithms).

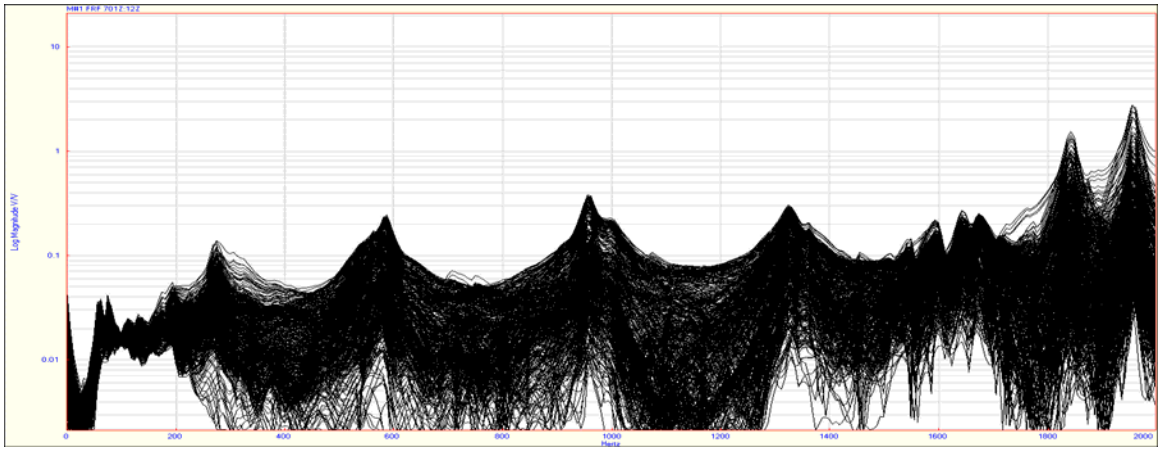

Figure 3.5 Overlaid FRFs from a roving excitation test on the undamaged I-beam

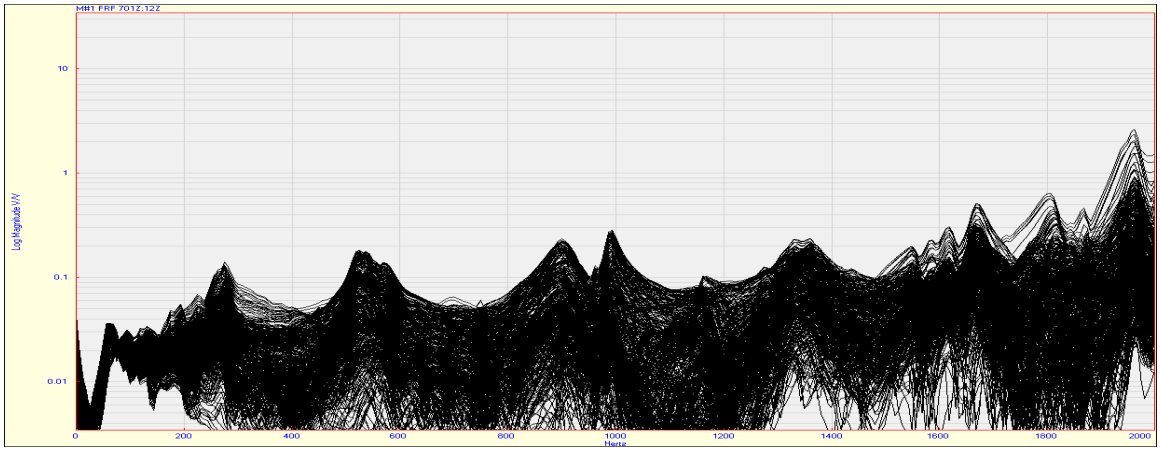

Figure 3.6 Overlaid FRFs from a roving excitation test on the I-beam with two masses

3.2.1.2 VBDI with Local Curve Fitting

As stated in Chapter 2, damage can be simulated by the addition of mass to a structure because mass is a dynamic property. Figure 3.7 shows the damage index (calculated using Eq 2.18) from a roving excitation test. The y-axis is position along the beam from 0 to 81 inches, and the x-axis is frequency shown in spectral lines. Warm colors represent the largest change in curvature between actual FRF test results and the curve fit FRF test results (using GSM), and white indicates virtually no change. The frequency range for this particular test was 10000 Hz at 1 line/6.25 Hz. The solid red lines indicate the boundaries of the large mass. Likewise, the dashed red lines indicate the boundaries of the small mass.

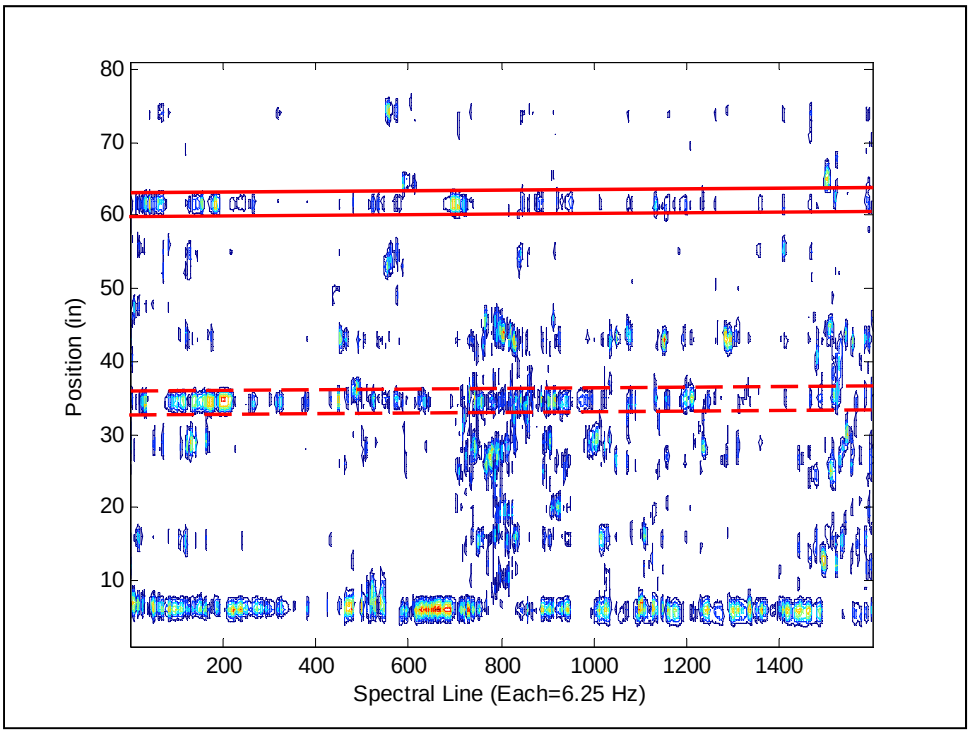

Figure 3.7 Damage index using difference between FRFs and GSM-fit FRFs

Figure 3.7 clearly indicates a large change in FRF curvature within both damage regions but also shows a thick band of color around 5-8 inches. Also present are thinner bands of color at various points along the structure. Figure 3.8 is the summed damage index (calculated using Equation 2.19), which sums the change in curvature along the entire frequency spectrum. Therefore, the x-axis is positioned along the beam and the y-axis is the magnitude of the summed damage index. Once again, the red lines indicate the damage boundaries, and

black lines were added to show the location of each accelerometer. Figure 3.8 not only locates the damage properly, but also shows a relationship between small intermediate peaks in summed damage index and accelerometer location: accelerometers at nodes 16, 43, 55, and 74 were located perfectly.

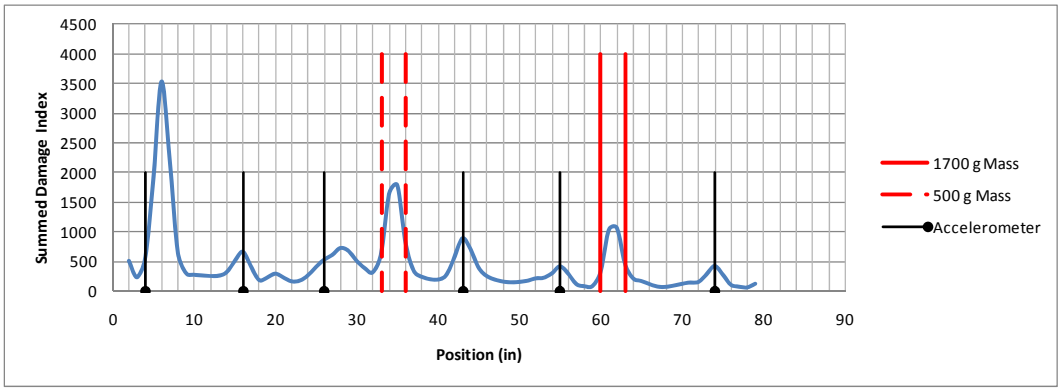

Figure 3.8 Summed damage index using difference between FRFs and GSM fit FRFs for all frequencies

The reasoning for the difference in FRF curvature at fixed accelerometer locations is not fully understood. The accelerometers have negligible mass compared to the cylinders fixed to the top flange of the beam and have no effect on the beam's damping or stiffness. Because the beam was impacted every inch, the impacts on nodes very close to a given accelerometer could be causing the change in curvature. For this particular structure, the false positive damage indication at each accelerometer can easily be suppressed with numerical techniques because their magnitude is less than that of the actual damage. For other structures, this could hold true, or the accelerometer locations could be subtracted from subsequent tests (i.e., accelerometers are placed in the same reference locations for various tests during a structure's life cycle, and results are subtracted so that accelerometer false positives disappear).

The large change in curvature between 5-8 inches indicated in both Figures 3.7 and 3.8 could be due to the fact that the accelerometer at node 4 is on a highly stiffened portion of the beam. As shown in Figure 3.5, the laboratory I-beam has stiffeners at both ends. The stiffener at the other end of the beam may not have been identified because the closest accelerometer was a few inches away, not directly on the stiffened part of the flange.

Unfortunately, both Figures 3.7 and 3.8 fail to properly quantify the severity of the damage relative to each other. The band of color in the damage index is thicker and darker in the region of the smaller mass, and the peak in the summed damage index is higher for the smaller mass. This is most likely due to the fact that the smaller mass was placed more toward the middle of the beam, where there is maximum deflection.

3.2.1.3 VBDI with Local and Global Curve Fitting

As stated in Chapter 2, GSM is a local curve fitting method, whereas MEscope software is capable of globally smoothing FRF test results. The results presented in this section represent a novel approach to smoothing data in damage detection. First the FRF data is globally smoothed in MEscope only within a region where a mode is well-defined (because global smoothing of the entire frequency spectrum fails to accurately curve fit the data). For this test, the third mode from 875-925 Hz was chosen (see Figure 3.6). Next, the curve fit data and actual data within this 50 Hz region are exported from MEscope and run through the normal FRF Curvature with GSM damage detection algorithm independently of each other. The squared difference of the summed damage index from the curve fit data and actual data is then calculated, as shown in Figure 3.9.

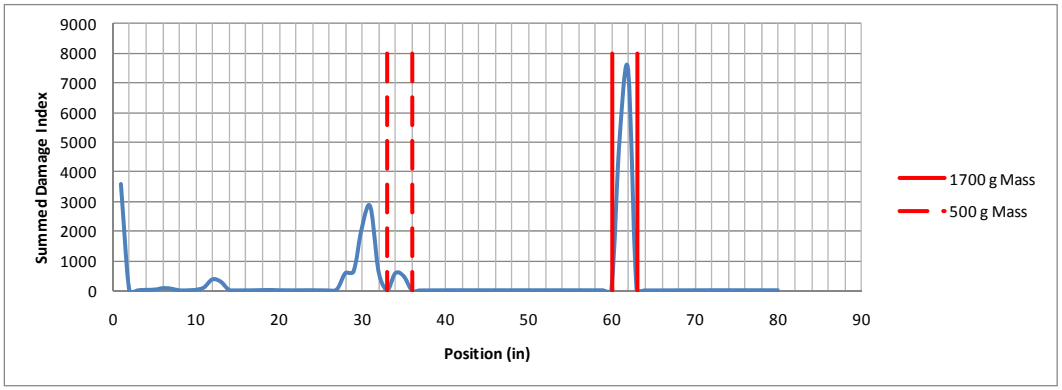

Figure 3.9 Summed damage index using difference between SMN-FRF and SMN-MEscope-fit FRFs for frequencies from 875-925 Hz

As Figure 3.9 shows, both areas of damage are accurately located, and the large mass between nodes 60-62 shows up with a magnitude significantly higher than that of the smaller mass. Also, the accelerometer locations no longer show up as damage because they have

effectively been subtracted out. The small peak around node 12 and the large peak around node 31 are false positives. They exist because in these locations the MEscope global curve fit did not accurately represent the actual data, either because better software parameters could be set or because the frequency range was too limited or extensive.

3.2.1.4 Effect of Nodal Mesh on VBDI with Local Curve Fitting

Three roving excitation tests with varying nodal meshes were completed on the I-beam with the same damage configuration as described in the previous two sections. Figures 3.10-3.12 show the 240, 120, and 84 overlaid FRFs from tests with 2 inch, 4 inch and 6 inch roving excitation point measurements. All three figures have approximately the same shape and natural frequencies, which is to be expected.

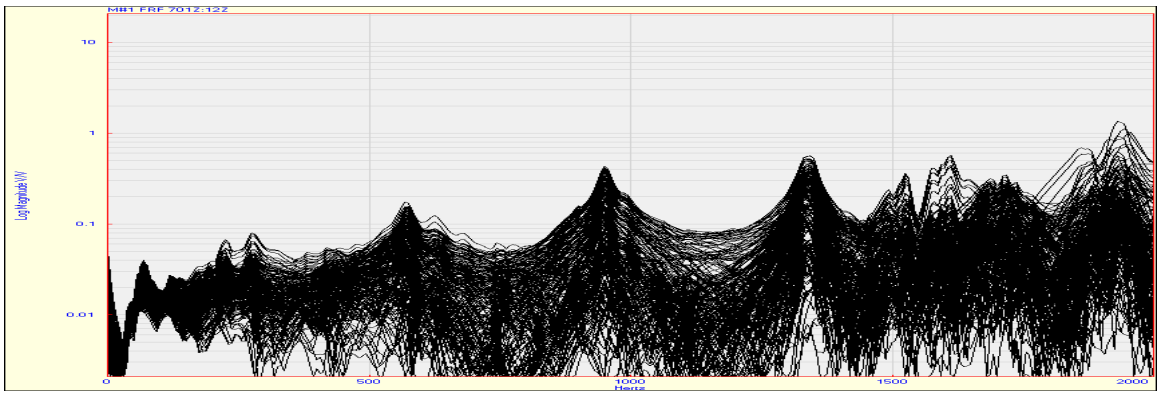

Figure 3.10 Overlaid FRFs from roving excitation test with two masses and 2 inch elements

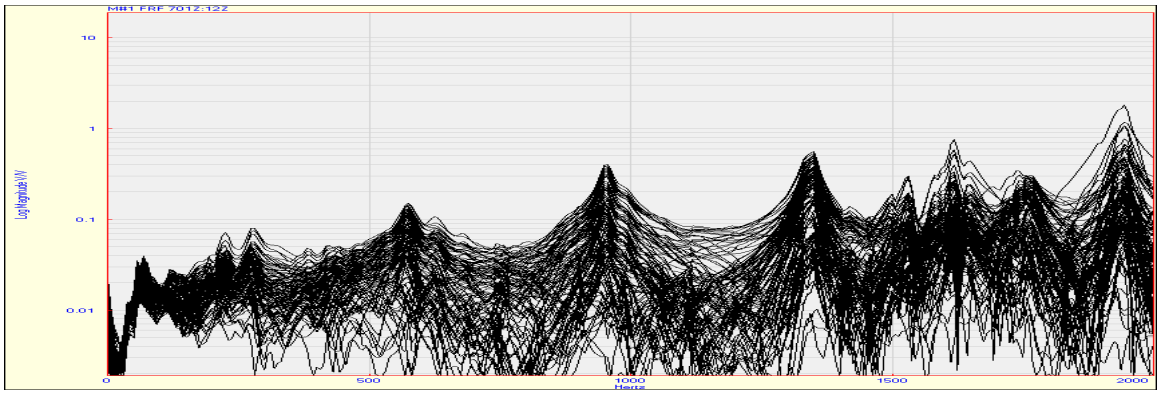

Figure 3.11 Overlaid FRFs from roving excitation test with two masses and 4 inch elements

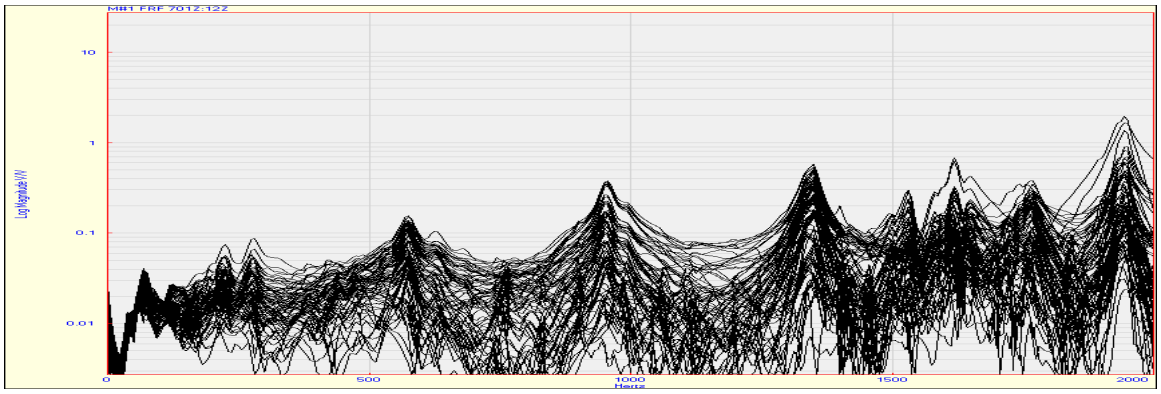

Figure 3.12 Overlaid FRFs from roving excitation test with two masses and 6 inch elements

Figures 3.13-3.15 show the summed damage indices for roving excitation tests with 2 inch, 4 inch, and 6 inch nodal meshes, respectively. Although not as smooth as the summed damage index from a nodal mesh of 1 inch, Figure 3.14 shows that the damage is still noticeable when exciting the beam every 2 inches. However, with this setup, the accelerometer locations are not identified as clearly as the fine mesh, which means it will be harder to account for their presence with numerical techniques. Also, the magnitude of the fourth accelerometer peak is actually greater than both damage locations. Both Figures 3.14 and 3.15 show that nodal meshes of one excitation point per 4 inches and 6 inches is not adequate to detect damage.

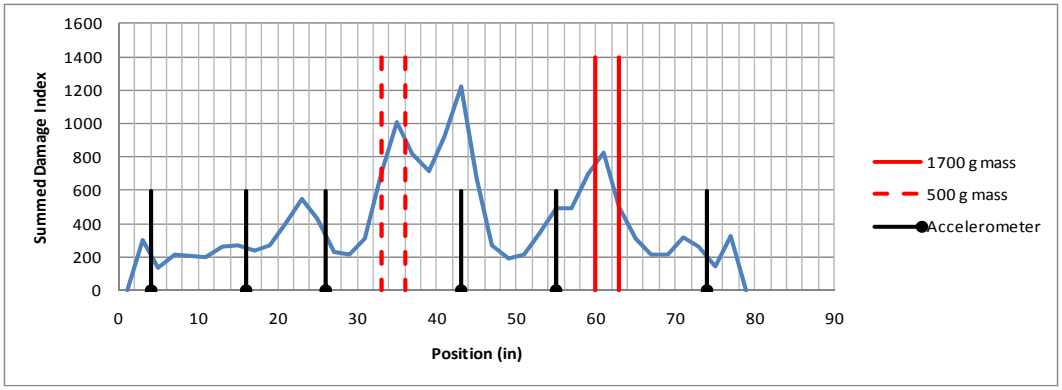

Figure 3.13 Summed damage index for roving excitation test using 2 inch elements

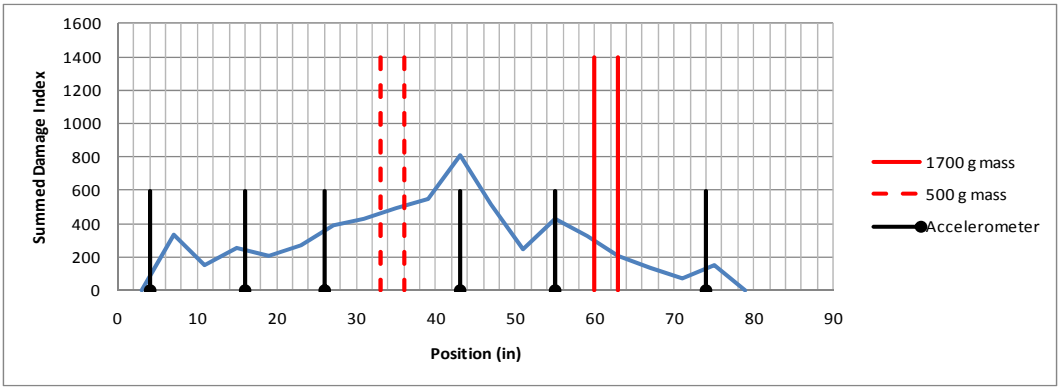

Figure 3.14 Summed damage index for roving excitation test using 4 inch elements

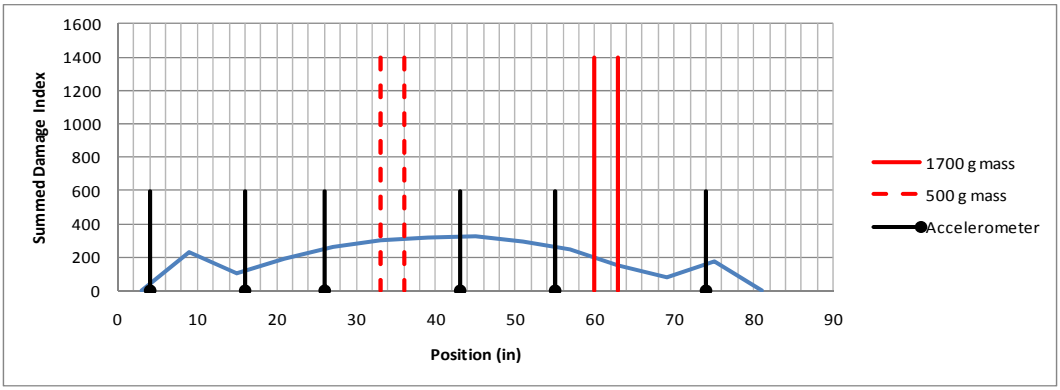

Figure 3.15 Summed damage index for roving excitation test using 6 inch elements

3.2.2 Forced Vibration Test with One Outer Flange Damage Location

Other damage locations and types were considered while testing the I-beam. In order to test the ability of the method to detect damage away from the centerline, 510 g clamps were fixed to the outer edge of the top flange at node 61 as shown in Figure 3.16. A roving excitation test similar to that shown in Figure 3.6 was run with this setup.

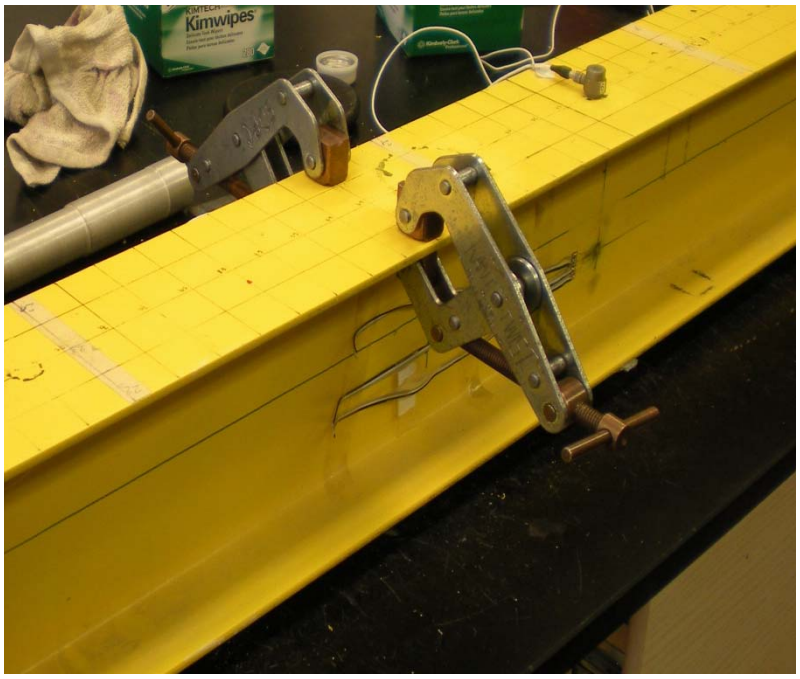

Figure 3.16 Clamps (510 g each) fixed to outer edge of top flange of beam at node 61

3.2.2.1 Identification of Clamps on Top Flange

Figure 3.17 shows the overlaid FRFs from 0-2000 Hz collected from a roving excitation test on the I-beam with clamps fixed to the top flange at node 61. Together, the 510 g clamps represent 3.7% of the beam's total mass.

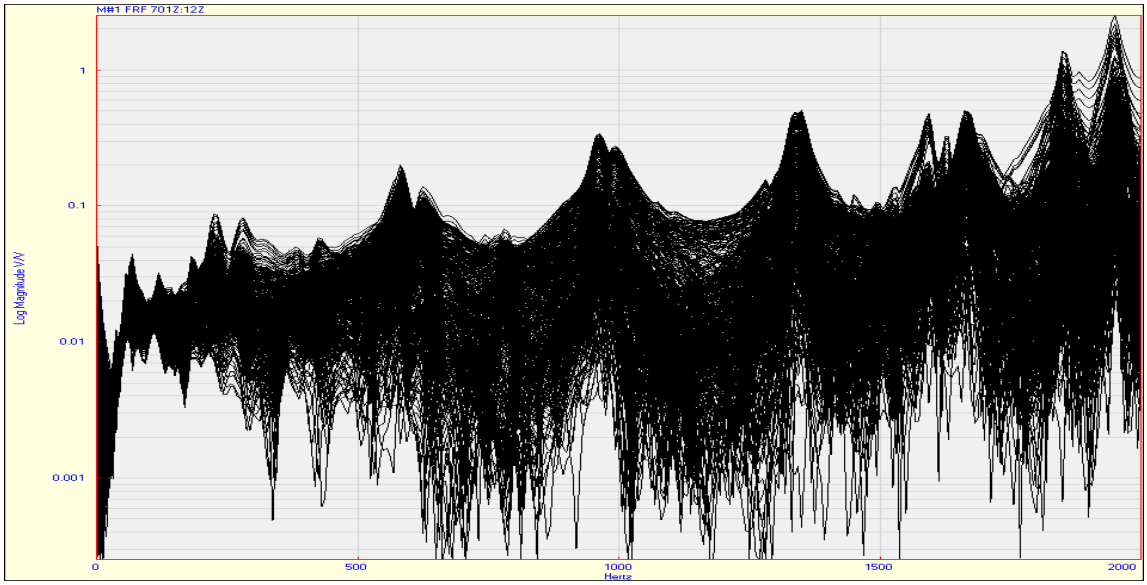

Figure 3.17 Overlaid FRFs from roving excitation test on I-beam with two clamps

3.2.2.2 VBDI with Local Curve Fitting

Figure 3.18 shows the damage index of a roving excitation test on the I-beam with two 510 g clamps fixed to the edges of the top flange at node 61. As shown, a thick band of color exists between nodes 60 and 62, indicating large changes in curvature between the experimental FRF and the smoothed FRF. Figure 3.19 shows the summed damage index with red lines for the region where the clamps were fixed and black lines indicating the locations of accelerometers. Once again, the accelerometer locations are clearly located with the roving excitation test method; however, the damage magnitude is 50% greater than the largest accelerometer peak.

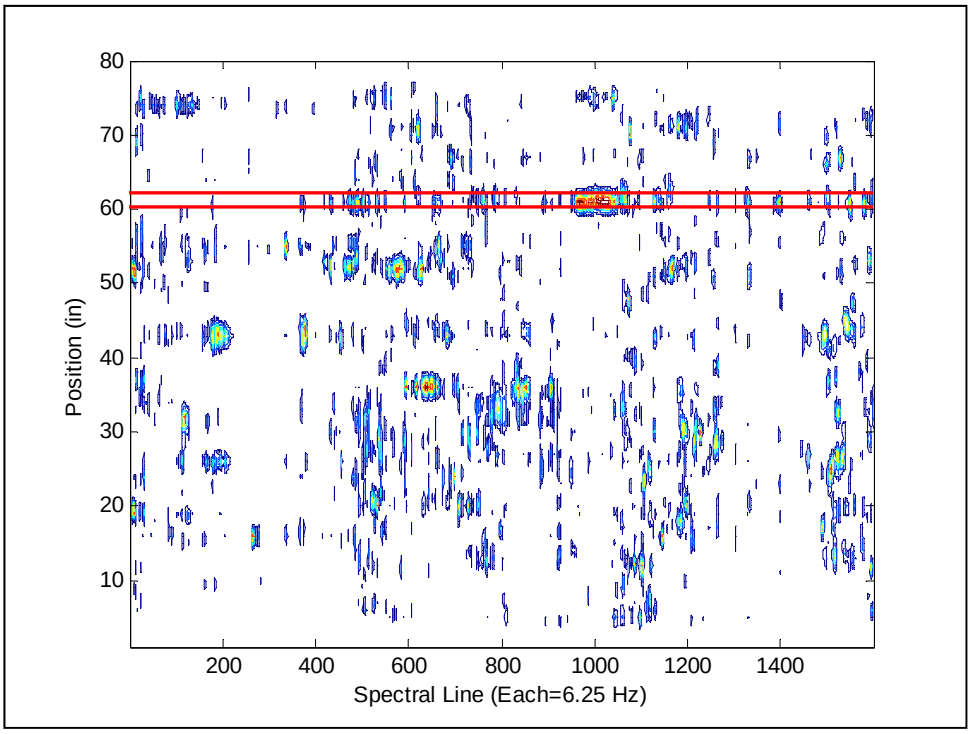

Figure 3.18 Damage index from roving excitation test on I-beam with two clamps at node 61

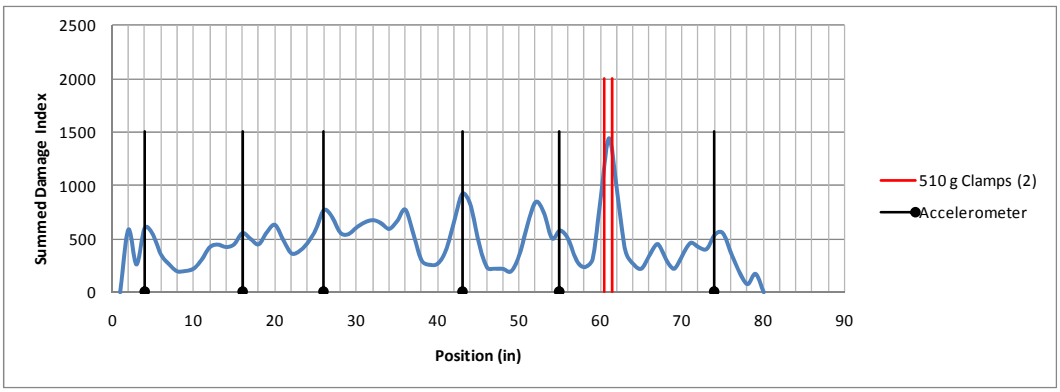

Figure 3.19 Summed damage index from roving excitation test on I-beam with two clamps at node 61

The ability to detect the clamps on the outer edge of the top flange is crucial because it shows that the identification of the two centerline masses was independent of the fact that impacts in the regions surrounding the masses were not actually on the centerline nodes. In the clamps test, added masses did not interfere with the centerline, so all nodes were impacted.

3.3 Scale Bridge

Laboratory testing was completed on a scale model of half of the FHWA # 31690 bridge. The model was constructed at approximately 1/6 scale and was made with two 10 foot long M6x4.4 junior I-beams and four 2 foot 6 inch long C3x3.5 channel sections, as shown in Figure 3.20. The channel sections were fixed to the I-beams with small angles and 1/4 inch bolts. Each bearing pad is made of two steel plates (3/4 inch and 1/2 inch thickness). One side of the model bridge utilizes a pintle in the top bearing plates, as does the actual bridge, to create a simply supported structure. Figure 3.21 shows the scale bridge in the laboratory.

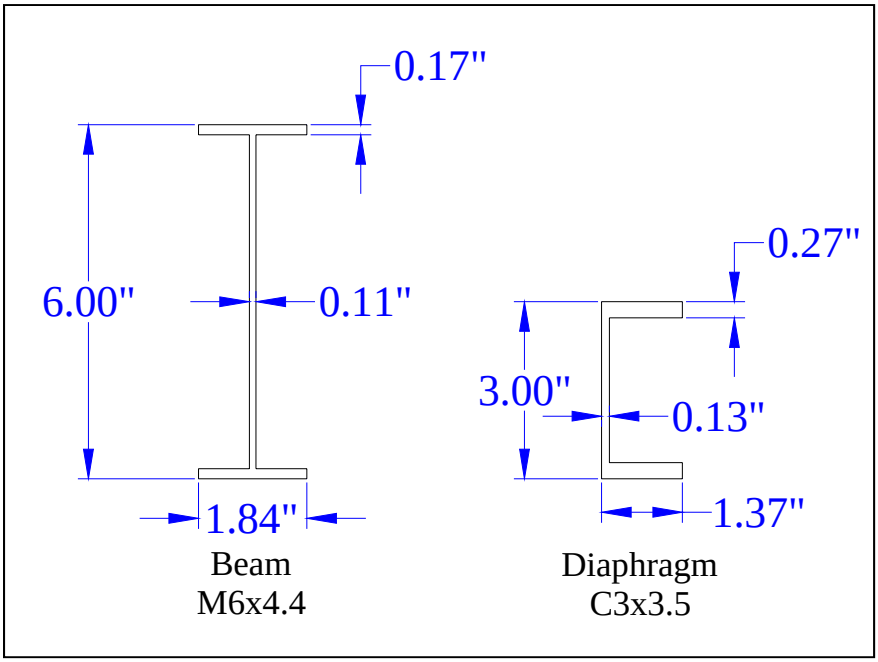

Figure 3.20 Scale bridge member cross sections

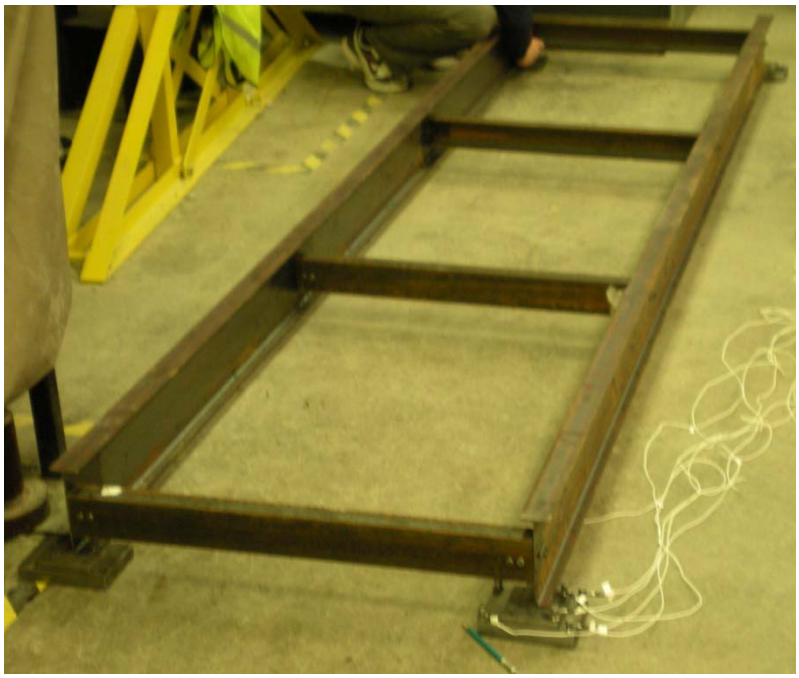

Figure 3.21 Scale bridge in the laboratory

3.3.1 Forced Vibration Test on Baseline Structure

Six uniaxial accelerometers were roved on the top flanges and bearing plates of each beam. A nodal mesh of one response point per six inches was used on the top flanges of the beams, and each corner of both end plates was measured for all four boundary conditions. The right beam was impacted in the downward vertical direction 20 inches from the end of the beam (node 12). Figure 3.22 shows a 3-D rendering of the structure with 98 labeled points (9 per boundary condition, 19 per beam, and 6 per diaphragm member), and Figure 3.23 shows a close-up of the right beam's first boundary condition with accelerometers on the first six response points. Frequencies from 0-10000 Hz were analyzed with a spectral density of 1 line/6.25 Hz.

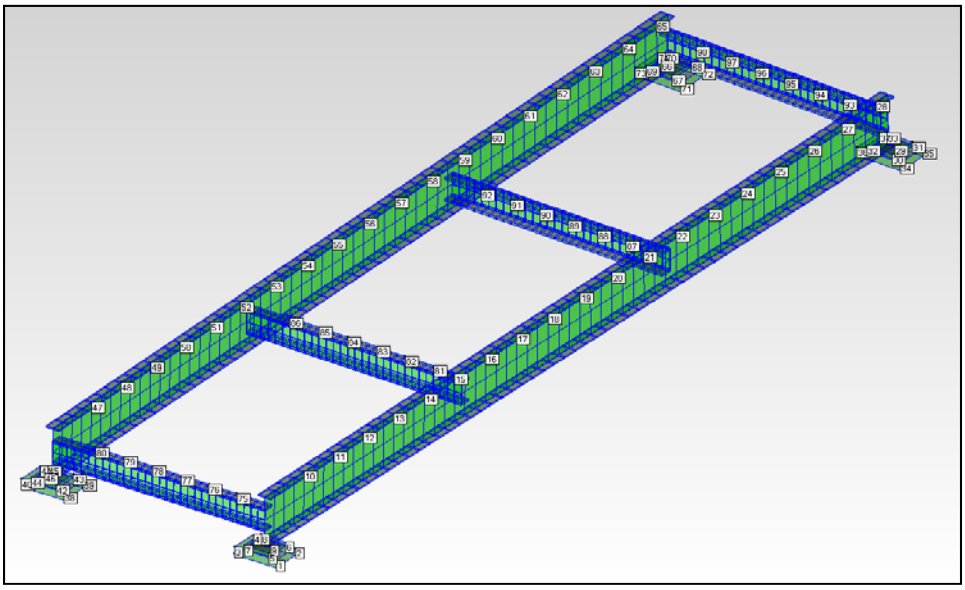

Figure 3.22 Rendering of scale bridge with 98 labeled response points

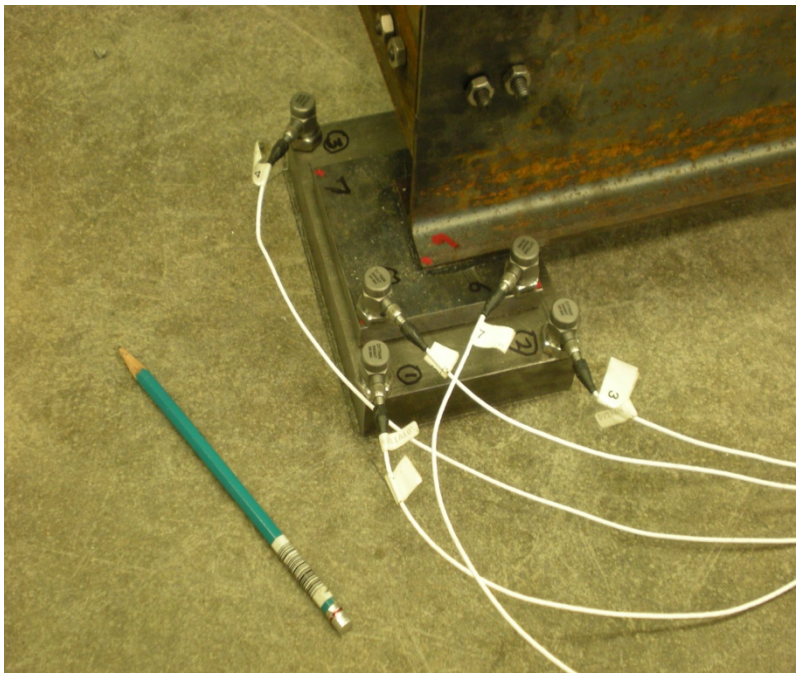

Figure 3.23 Accelerometers on the first six response points of the scale bridge

3.3.1.1 Identification of Stiffened Areas

Figure 3.24 shows the overlaid FRFs from 0-2000 Hz collected from a roving response test on the scale bridge with no added damage. Some of the FRFs appear to have little agreement with the others because there were response points on various substructures such as end plates and diaphragm members.

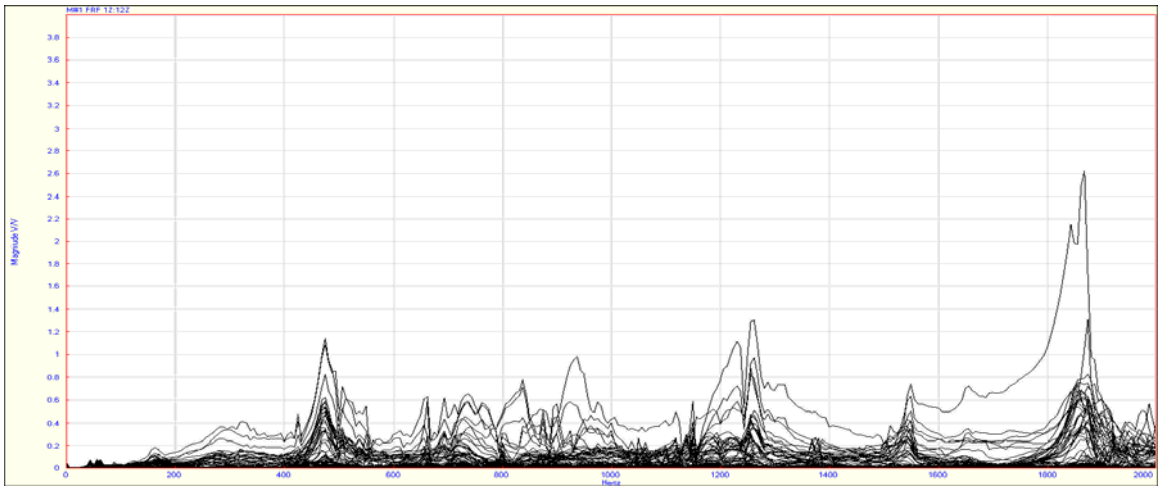

Figure 3.24 Overlaid FRFs from forced excitation, roving response test on baseline scale bridge

3.3.1.2 VBDI with Local Curve Fitting

Figures 3.25 and 3.26 show the damage indices for response points on the right and left beams, respectively. The solid red lines indicate the location of the intermediate diaphragm members at the third points of the 10 foot long beams. With no damage added to the structure, the use of a local curve fitting method should only show areas of the beam that are highly stiffened. The regions of color in Figures 3.25 and 3.26 are mostly within the intermediate diaphragm members, but also extend out past the channel sections for approximately 1 foot on each side. Therefore, for this structure with intermediate diaphragm members at third points, the stiffened region due to those members covers approximately the middle two-thirds of the structure.

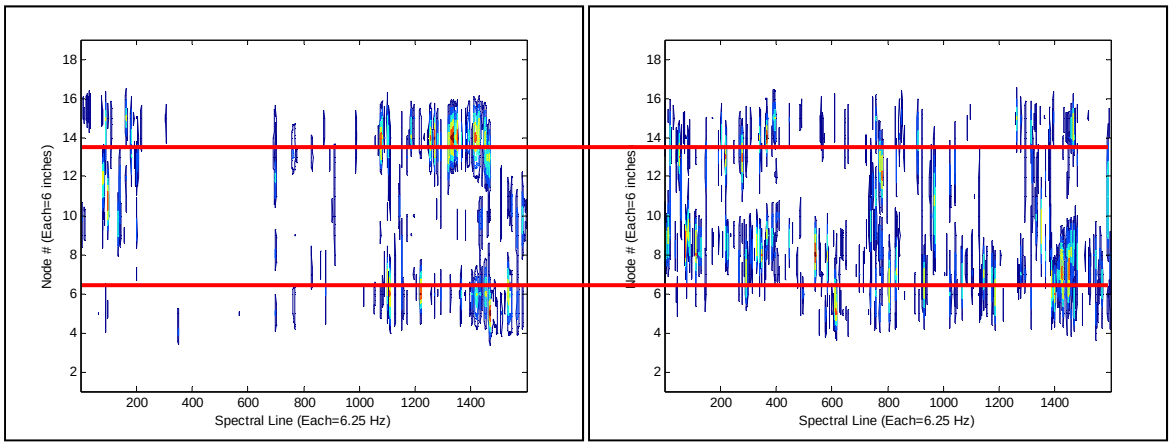

Figure 3.25 Damage index for right beam of baseline scale bridge and Figure 3.26 Damage index for left beam of baseline scale bridge

3.3.2 Forced Vibration Test with One Damage Location

Damage was added to one of the beams of the scale bridge to determine if the highly stiffened region in the middle of the structure has an effect on damage detection using the FRF curvature method. For this experiment, a 1500 g mass was fixed to the top flange of the right beam 20 inches from the far end (on node 16), as shown in Figure 3.27. This mass represents 3.2% of the total structure's mass (excluding the bearing plates) and 7.5% of the right beam only. Response points for this test were the same 98 points shown in Figure 3.22.

Figure 3.27 Mass (1500 g) added to top flange of beam 1, 20 inches from the far end

3.3.2.1 Identification of Mass

Figure 3.28 shows the overlaid FRFs from 0-2000 Hz collected from a roving response test on the scale bridge with the added damage. Once again, some of the FRFs appear to have little agreement with the others because there were response points on various substructures such as end plates and diaphragm members.

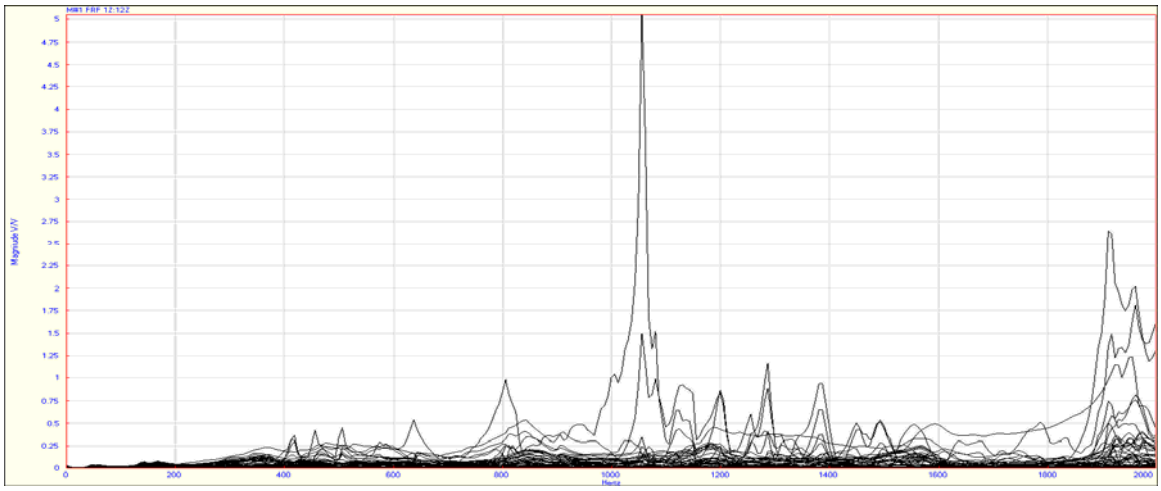

Figure 3.28 Overlaid FRFs from forced excitation, roving response test on damaged scale bridge

3.3.2.2 VBDI with Local Curve Fitting

Figures 3.29 and 3.30 show the damage indices for response points on the right and left beams, respectively. The solid red lines indicate the location of the intermediate diaphragm members at third points of the 10 foot long beams. The dashed black line in Figure 3.29 indicates the location of the mass. With no damage added to the left beam, the use of a local curve fitting method should only show areas of the beam that are highly stiffened. The regions of color in Figure 3.30 are mostly within the intermediate diaphragm members, but also extend out past the channel sections for approximately 1 foot on each side, exactly as with the baseline test. However, Figure 3.29 shows a much more random color distribution with no discernable pattern in curvature change. The stiffened middle area is no longer visible on the damage index for the right beam, and the impact point at node 2 is clearly visible. Unfortunately, although the method clearly indicates a difference in curvature change for the beam as a whole, it was unable to locate the damage at node 16.

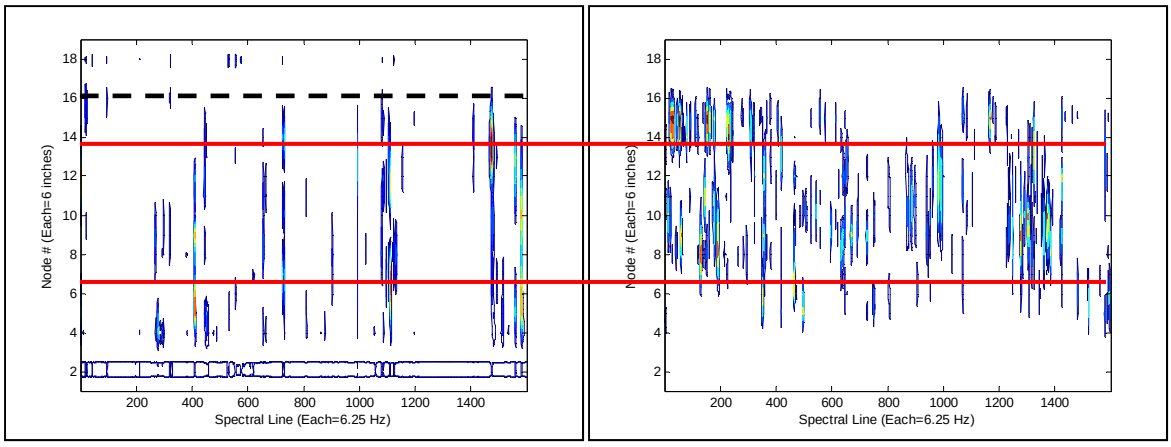

Figure 3.29 Damage index for damaged right beam of scale bridge and Figure 3.30 Damage index for undamaged left beam of baseline scale bridge

3.3.3 Global Operational Vibration Test with One Damage Location

To simulate operational traffic load on the scale bridge structure, the top flange of each beam was impacted once in the vertical direction at five different locations. Therefore, each data set is composed of 10 averaged impacts. The impact locations were at 20, 40, 60, 80, and 100 inches from the near end of both beams. Although the impact hammer was used to

excite the structure, it was not used as a reference because the goal of the experiment was to simulate an operational environment where the excitation is difficult or impossible to measure. Therefore, a reference accelerometer was fixed to the top flange of the right beam at its midpoint. The roving response points were the same for this experiment as shown in Figure 3.23.

3.3.3.1 Analysis of Real Motion of Structure

Figure 3.31 shows 98 overlaid ODSFRFs from 0-500 Hz. By assigning the 98 ODSFRFs in Figure 3.31 to their actual measurement points as shown in Figure 3.23, the actual motion of each point of the structure relative to the reference response at the midpoint of the first beam can be calculated and animated using MEscope software. This allows users to visualize the effect of an average "operational load" traversing the scale bridge.

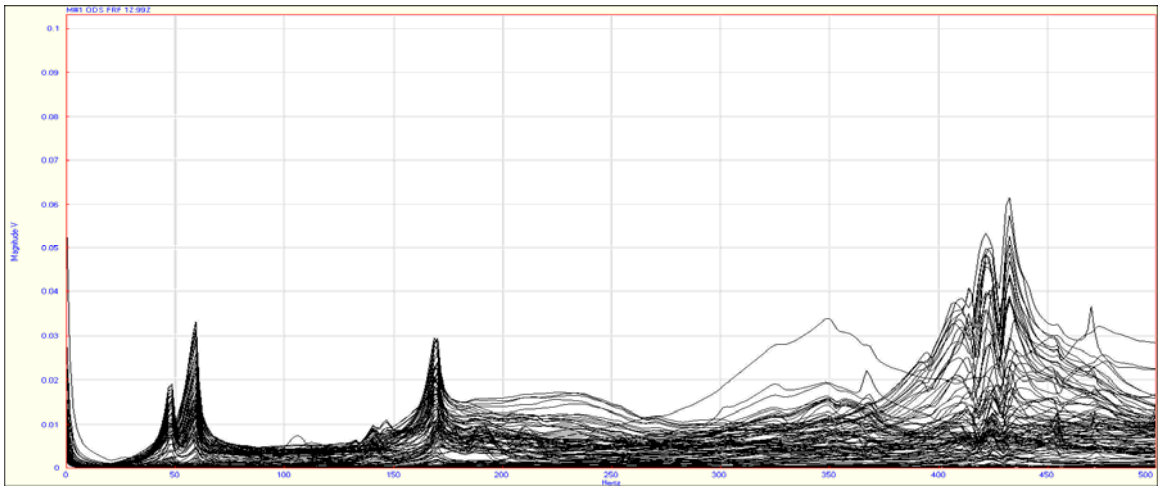

Figure 3.31 Overlaid FRFs from operational vibration, roving response test on damaged scale bridge

Figure 3.32 shows a screenshot of the animation of the ODSFRFs at 46.9 Hz, which causes the beams to experience first mode bending. At frequencies around the first mode shape, the diaphragm members experience various levels of first mode bending activity, but at the frequency shown they remain straight because both beams are bending with almost identical shapes. Figure 3.33 shows a screenshot of the animation of the ODSFRFs at 59.4 Hz, which causes the beams to experience first mode bending with a phase change (i.e., when right beam midpoint is minimum, left beam midpoint is maximum). Assuming a deck were

present on top of the beams, it can be inferred that if the structure was often excited at this frequency, it would cause significant lateral cracking in the deck.

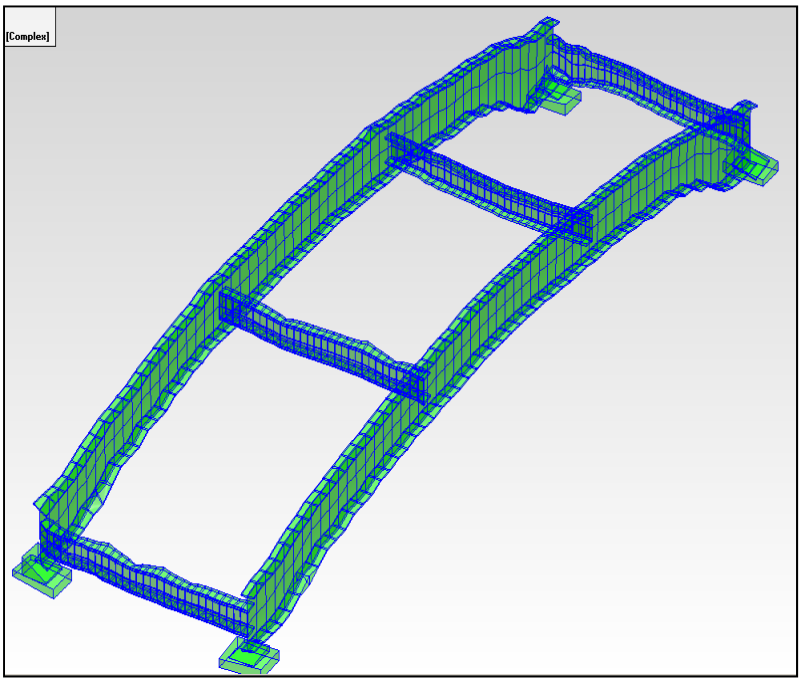

Figure 3.32 Screenshot of MEscope animation of scale bridge ODSFRFs at 46.9 Hz

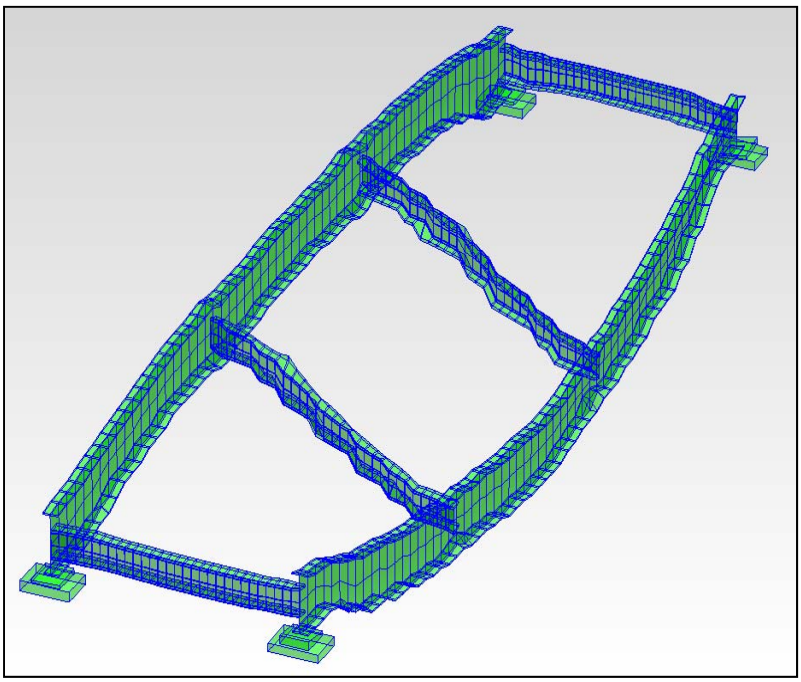

Figure 3.33 Screenshot of MEscope animation of scale bridge ODSFRFs at 59.4 Hz

4. FIELD EXPERIMENTS

Field testing was completed on FHWA # 31690, a composite steel girder and concrete deck single span bridge. The bridge carries HWY 1 over a small natural creek between Black Diamond Road and Gingerich Road in Johnson County, Iowa. Having been constructed in 1949, the bridge has been rated functionally obsolete by Iowa DOT inspectors but is not structurally deficient and has an overall sufficiency rating of 37 (Iowa Department of Transportation). Spanning approximately 61 feet, the structure is primarily composed of four steel girders, a diaphragm with twelve channel members, and an 8 inch concrete deck. The exterior steel girders are W33x150, the interiors are W36x150, and the channels are C15x33.9 sections. Figure 4.1 shows a plan view of the bridge, and Figure 4.2 shows the member cross sections. Field investigations were carried out during two test dates: November 2009 and April 2010.

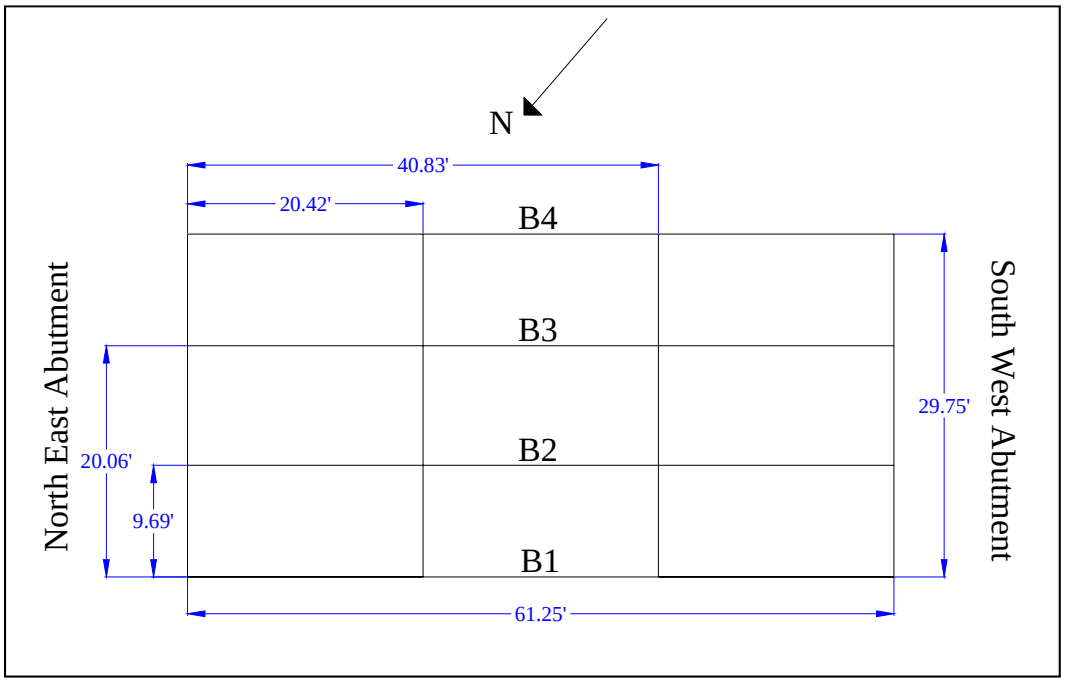

Figure 4.1 Plan view of FHWA # 31690

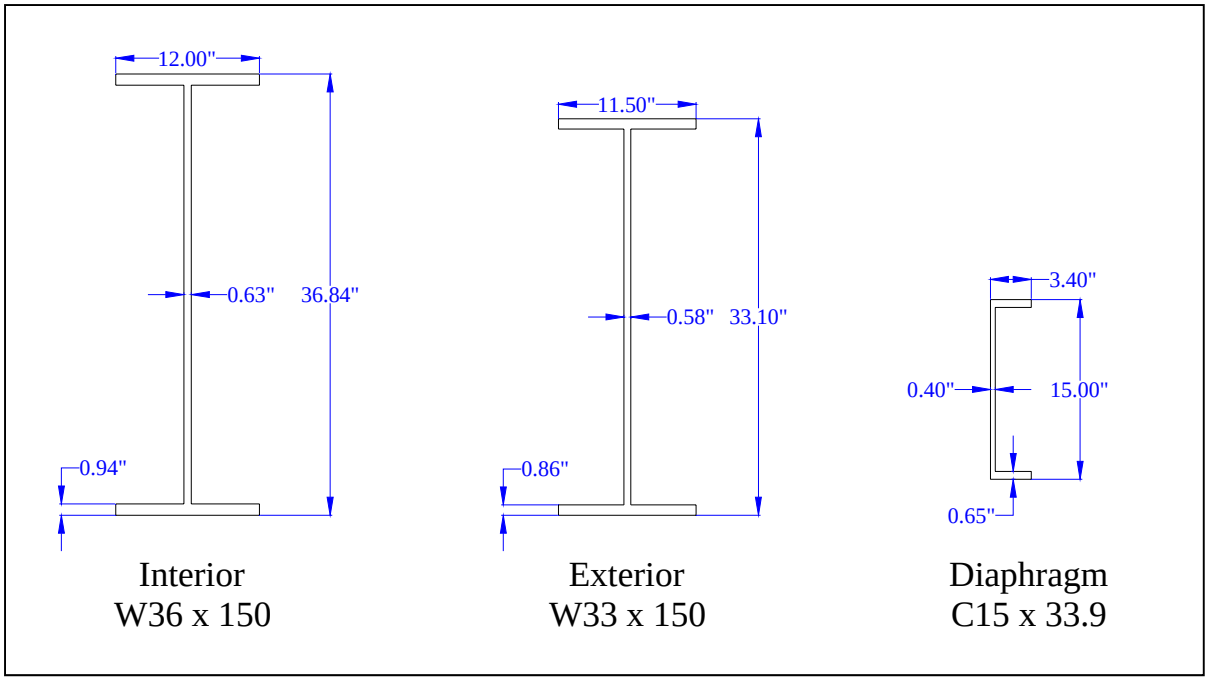

Figure 4.2 Schematic of member cross sections

4.1 Equipment

In the field a 5000 lbF range impulse hammer was used to excite the bridge. Three 5000 g range Dytran triaxial accelerometers and six 100 g range Dytran uniaxial accelerometers were used to determine the dynamic response of various structural elements. Typically, accelerometers were fixed to structures with a magnet, however in some cases wax was used with a magnet. An IOtech ZonicBook/618E Data Analyzer and an IOtech/650U were used to acquire data and construct FRF's. MEscope software was used to calculate mode shapes and ODSFRFs as well as to animate data. MATLAB was used to implement VBDI algorithms. Figure 4.3 shows a typical field operational vibration test setup.

Figure 4.3 Typical field operational vibration test setup

4.2 November 2009 Testing

The focus of this field investigation was to mark the steel girders to create a nodal mesh and acquire preliminary data for the entire bridge that could be used with the FRF Curvature Method. With the help of a DOT Snooper Truck, each steel girder was marked at one foot intervals on the bottom flange and web, as shown in Figure 4.4. One scaffolding tower was constructed under part of beam 1 so that the 12^{th} node on that beam could serve as the fixed excitation point for the entire bridge, as shown in Figure 4.5.

Figure 4.4 Markings at one foot intervals on the web and bottom flange of each beam

Figure 4.5 Single scaffolding tower used to impact beam 1 at node 12

One triaxial accelerometer was roved per beam to each node on the bottom flanges, and the excitation point on beam 1 was impacted both in the lateral (out of plane) and vertical directions. Response data was collected in the lateral and vertical directions. Frequencies

from 0-250 Hz were analyzed with a spectral density of 1 line/0.5 Hz. Figure 4.6 shows a schematic of the test setup for beam 1, and Figure 4.7 shows how the accelerometers were roved around the bridge. During this test, the DOT Snooper Truck was present on the bridge deck during the entire testing period in order to provide access to the girders.

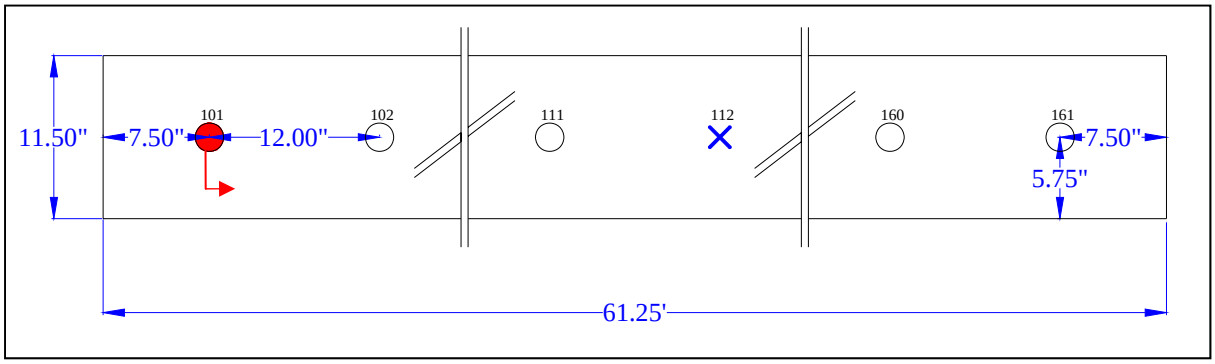

Figure 4.6 Schematic of forced vibration roving accelerometer test setup for bottom flange of beam 1 (one accelerometer per beam and impact point is stationary on beam 1 only)

Figure 4.7 Snooper truck and long poles used to access the bottom flange of each beam

4.2.1 Global Forced Vibration Beam Test

Figure 4.8 shows 228 overlaid vertical direction FRFs from 0-125 Hz (57 FRFs per beam). Although all these FRFs were measured together, having a common excitation point of node 12 on beam 1, for damage detection purposes FRFs for each beam are considered separately. Figures 4.9-4.12 show the damage indices for beams 1-4, respectively, with red lines indicating the location of intermediate diaphragm members. All results shown use the FRF curvature method with GSM only.

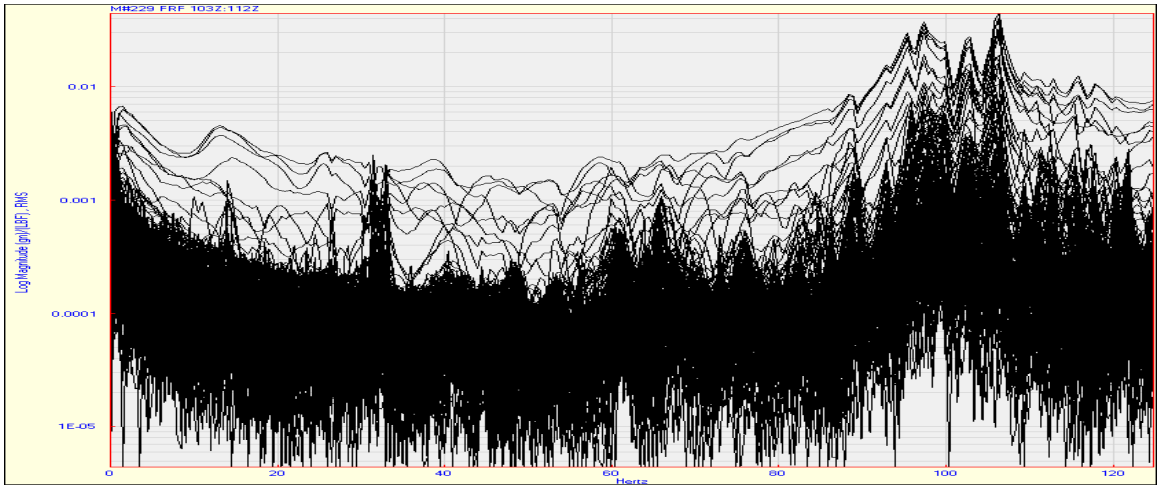

Figure 4.8 Overlaid FRFs from roving response test on all four beams of field bridge

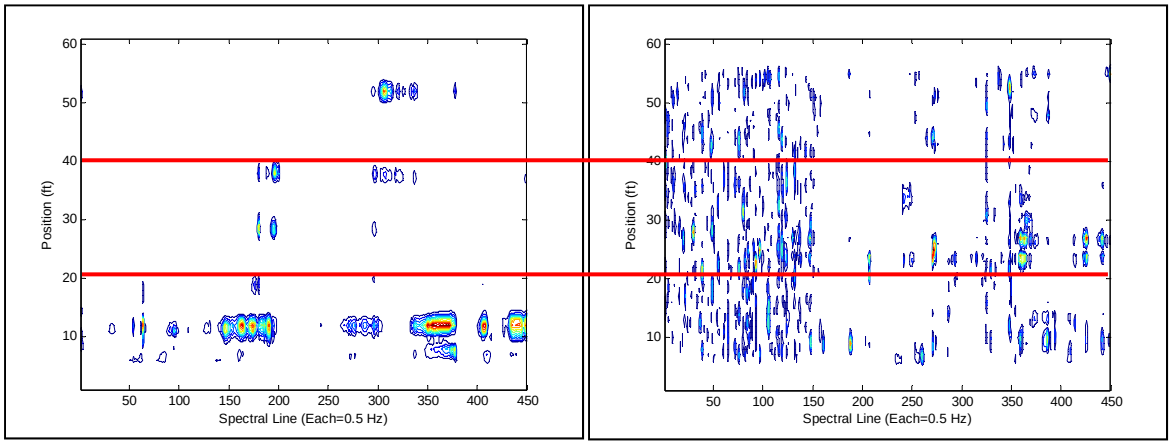

Figure 4.9 Damage Index for beam 1 and Figure 4.10 Damage Index for beam 2

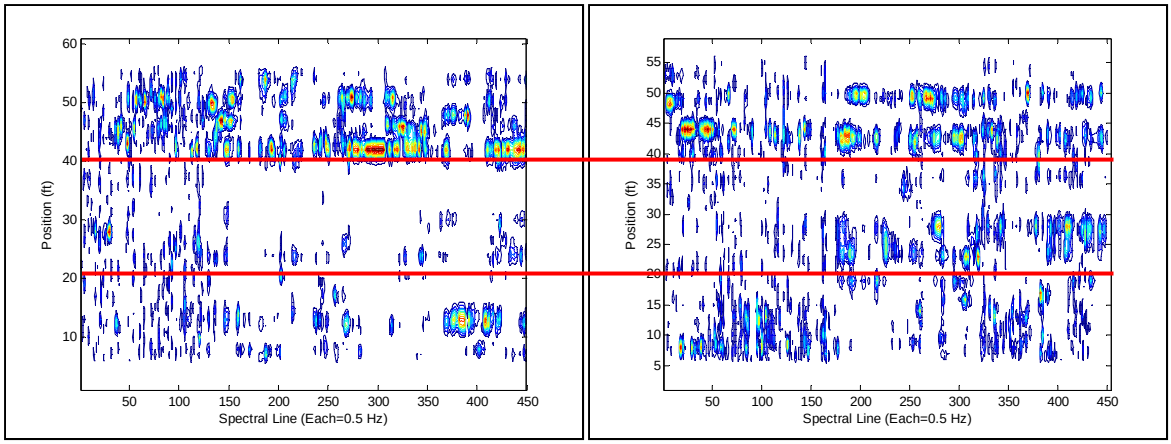

Figure 4.11 Damage index for beam 3 and Figure 4.12 Damage Index for beam 4

Figure 4.9 shows the impact location 12 feet from the end of the beam and is much clearer than the rest of the damage indices. The damage index in Figure 4.9 also shows a stiff/damped region close to the first and second intermediate diaphragm members as well as in the middle of the structure and approximately 8 feet from each end. It is difficult to assess the effect of the 28 ton DOT Snooper truck on the damage index for beam 1. The change in FRF curvature at locations 8 feet from the end of the first beam could be due to the truck weight.

Because the structure was excited on beam 1, the vibration dissipates significantly before it reaches the rest of the beams due to significant damping in the structure. It can be assumed that the DOT Snooper truck magnified this damping. Therefore, Figures 4.10-4.12 represent data largely affected by noise, and very little information can be gathered from them.

4.3 April 2010 Testing

The focus of this field investigation was much broader than the November test. The goal was to acquire enough data (both forced vibration and operational vibration data) to fully analyze the girders, diaphragm members, boundary conditions, and abutments. To accomplish these tasks, scaffolding was constructed beneath the entire structure, as shown in Figure 4.13. This eliminated the need for a large Snooper truck to be on the bridge deck during testing.

Figure 4.13 Scaffolding that provided access to the entire superstructure

4.3.1 Independent Forced Vibration Beam Test

The first test that was ran was a forced vibration test where the bottom flange of each beam's measured response was gathered independent of the rest of the structure. Beam 1 was impacted at node 16 and three accelerometers were roved every foot until the end of the beam, as shown in Figure 4.14. Figure 4.15 shows the equipment setup and the excitation of a beam. This process was repeated for each beam, yielding four independent forced vibration tests with 61 measurements each.

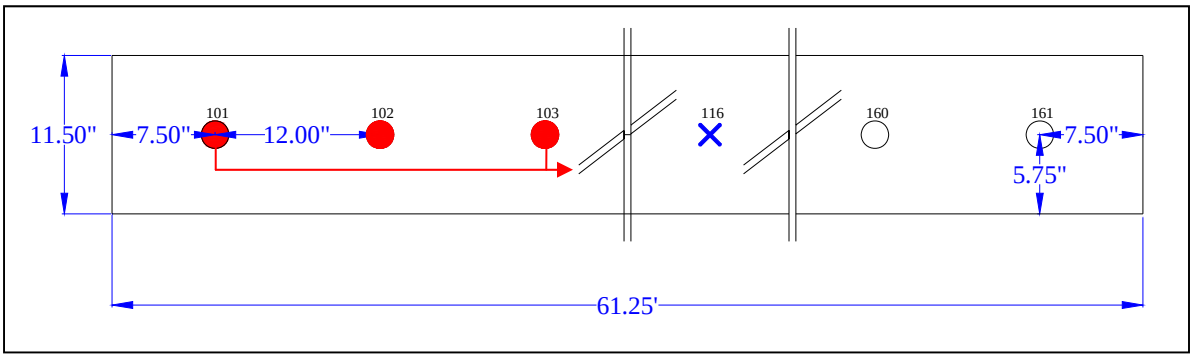

Figure 4.14 Schematic of forced vibration roving accelerometer test setup for bottom flange of beam 1 (three accelerometers per beam and impact point is on node 16 of each beam)

Figure 4.15 Data acquisition system setup with large impact hammer used to excite each beam

4.3.1.1 VBDI with Local Curve Fitting

FRFs from 0-125 Hz gathered from four independent forced vibration beam tests are shown in Figures 4.16-4.19. Because each of these FRFs was taken with its own excitation point (16 feet from end of beam for each), the FRFs shown are much clearer than the FRF in Figure 4.8, especially in the first 60 Hz. All four FRFs show many closely spaced, low-frequency modes. The shape of the FRFs for the exterior beams (4.16 and 4.19) are very similar to each other and indicate very clear modes until approximately 85 Hz. Likewise, the shape of the FRFs for the interior beams (4.17 and 4.18) are similar to each other but seem to indicate less natural frequencies.

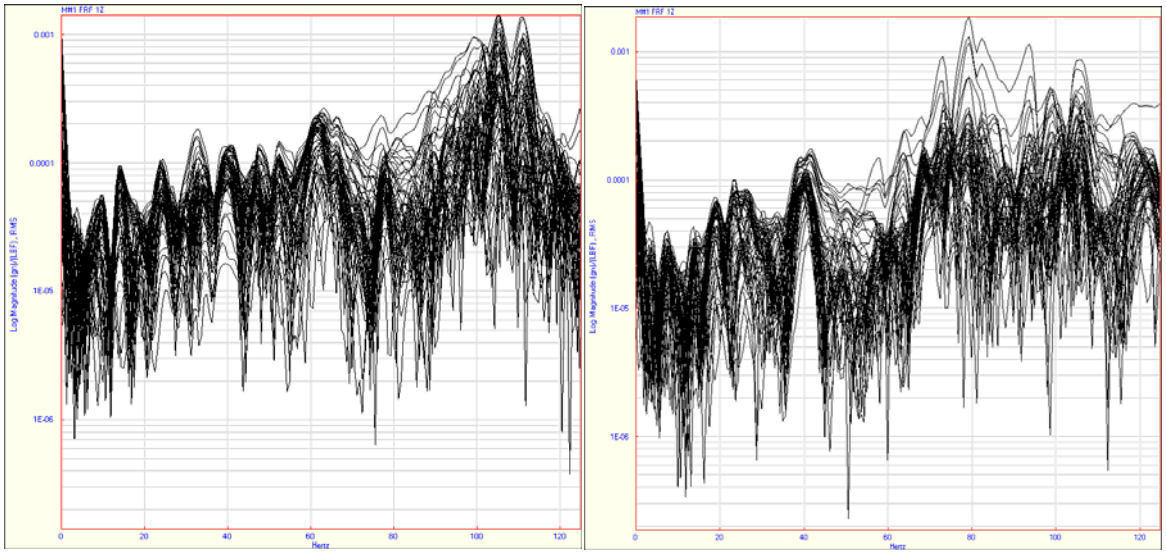

Figure 4.16 Overlaid FRFs for roving response test on beam 1 and Figure 4.17 Overlaid FRFs for roving response test on beam 2

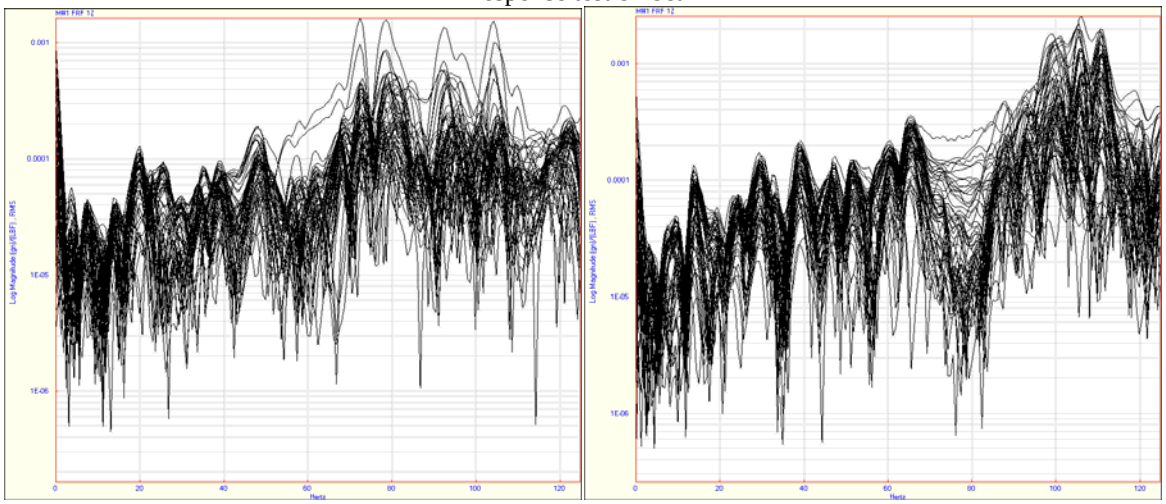

Figure 4.18 Overlaid FRFs for roving response test on beam 3 and Figure 4.19 Overlaid FRFs for roving response test on beam 4

Figures 4.20-4.23 show the damage indices for beams 1-4, respectively, with red lines indicating the location of intermediate diaphragm members. All results shown use the FRF curvature method with GSM only. All four damage indices in Figures 4.20-4.23 show the presence of the impact location near node 16 very clearly. Damage indices for the exterior beams (1 and 4) seem to show a line of curvature change near the intermediate diaphragm members. Unfortunately, besides the impact location, there is very little difference in FRF curvature at all other points in the interior beams, including regions close to the intermediate diaphragm members. Although the method of impacting each beam independently has

produced very high-quality FRFs, it does not seem robust in its ability to detect areas of high stiffness and may not be capable of detecting damage on large structures.

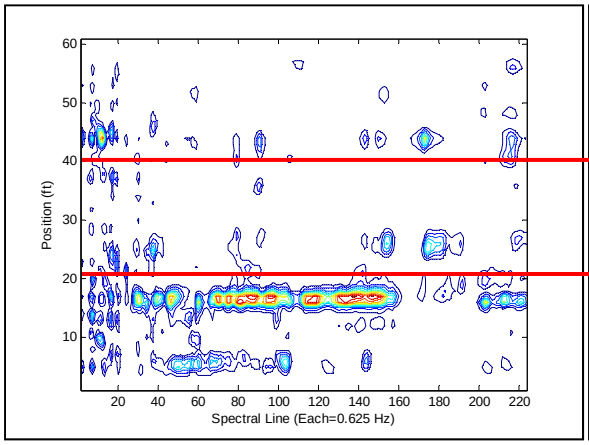

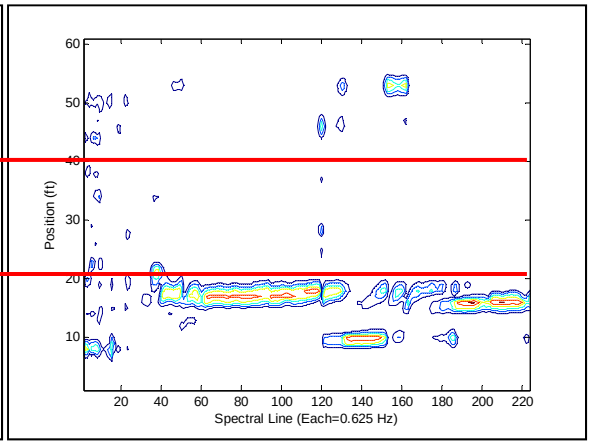

Figure 4.20 Damage index for beam 1 and Figure 4.21 Damage index for beam 2

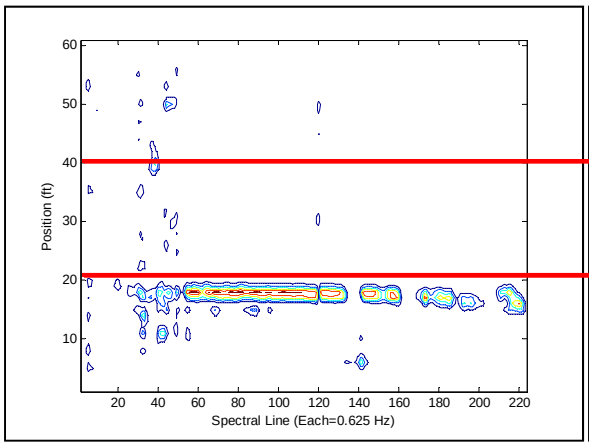

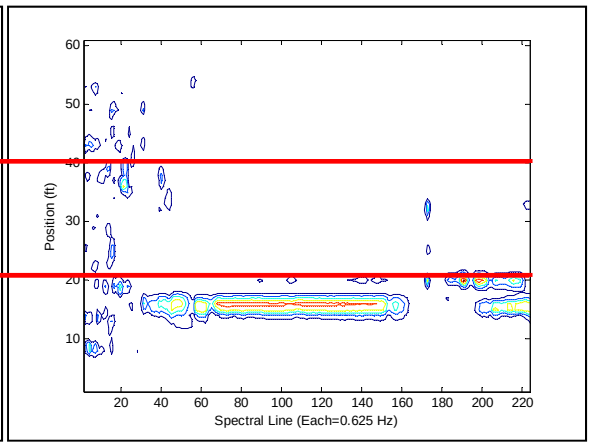

Figure 4.22 Damage Index for beam 3 and Figure 4.23 Damage Index for beam 4

4.3.2 Global Operational Vibration Bridge Test

The second test that was run in April 2010 was an operational vibration test where the majority of the structure was measured together. Figure 4.24 shows a 3-D rendering of the bridge with 440 labeled points (70 per beam, 10 per diaphragm, and 20 per abutment). Traffic loading was used as the operational vibration, and measurement was triggered by a reference accelerometer that was fixed to the bottom flange of the third beam at midspan (see

4.24A). A ten car average was used, meaning that after ten automobiles triggered the reference accelerometer, the response accelerometers were moved to the next measurement location. Five uniaxial accelerometers were used as response accelerometers and roved around the structure, including each girder, each diaphragm member, and the abutment wall. The nodal mesh on the beams was one measurement point per four inches for the two feet extending out from each end (see 4.24B) and one measurement point per foot for the remaining length of the beam (see 4.24C). The nodal mesh for each diaphragm member was one measurement per foot (see 4.24D). The nodal mesh for the abutment was one measurement per four inches directly below each beam for 20 inches (see 4.24E). This setup yielded one operational vibration test with 440 measurements. Figures 4.25 through 4.27 show the operational vibration response measurement of a beam, diaphragm member, and strip of abutment, respectively.

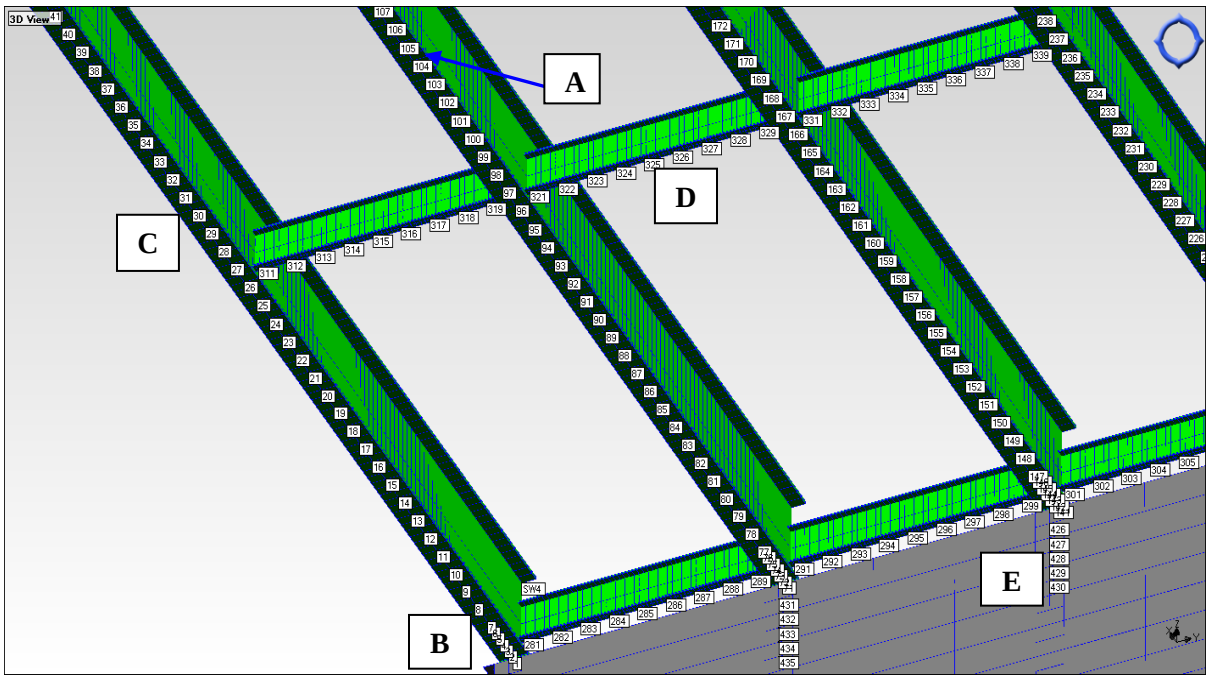

Figure 4.24 Rendering of the bridge with the reference response location (A), concentrated beam mesh near boundary conditions (B), normal beam mesh (C), diaphragm member mesh (D), and abutment mesh (E)

Figure 4.25 Operational vibration response measurement of a beam near the boundary condition

Figure 4.26 Operational vibration response measurement of a diaphragm member

Figure 4.27 Operational vibration response measurement of a strip of the vertical face of an abutment

4.3.2.1 Operational VBDI with Local Curve Fitting

Figure 4.28 shows 440 overlaid ODSFRFs from 0-125 Hz (70 per beam, 10 per diaphragm, and 20 per abutment). The ODSFRFs with magnitudes much lower than the others are from response points on the abutments, which were excited less by the traffic load. Because the abutment data sets consisted of eight placements of five response points each, not enough data was obtained in each placement to calculate meaningful damage indices. Damage detection algorithms were used on beam and diaphragm ODSFRFs extracted from the data shown in Figure 4.28.

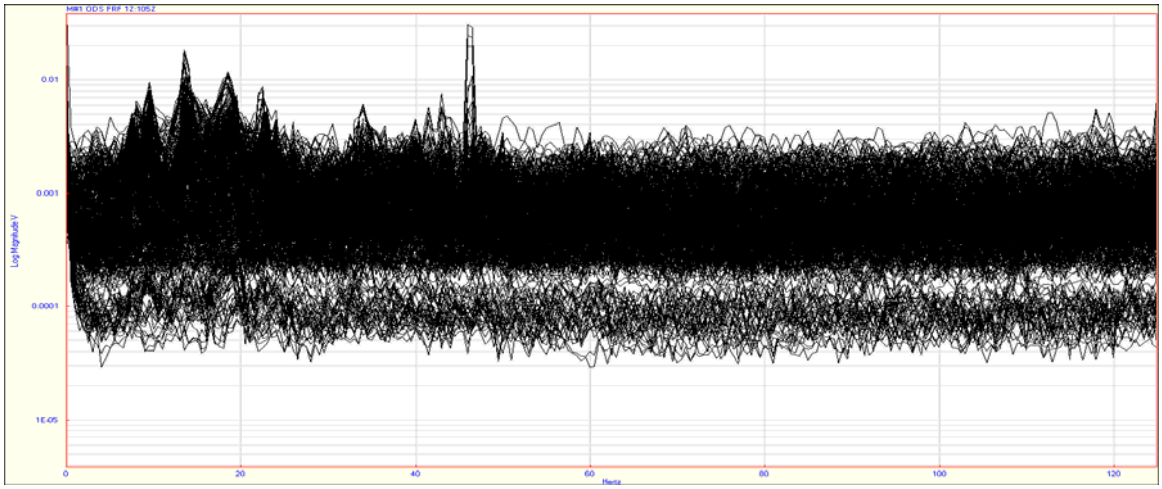

Figure 4.28 Overlaid ODSFRFs from global operational vibration test

4.3.2.2 Beams

Figures 4.29-4.32 show summed damage indices for beams 1-4, respectively. The summed damage indices of the exterior beams in Figures 4.29 and 4.32 show a distinct increase in ODSFRF curvature around and in between the intermediate diaphragm members, shown with solid red lines. This is to be expected, due to the significant addition of stiffness to the region around each diaphragm member. However, the interior beams show a much more spread out region of changed ODSFRF curvature. This could be due to a larger area of high stiffness caused by diaphragm members on either side of an interior beam's web.

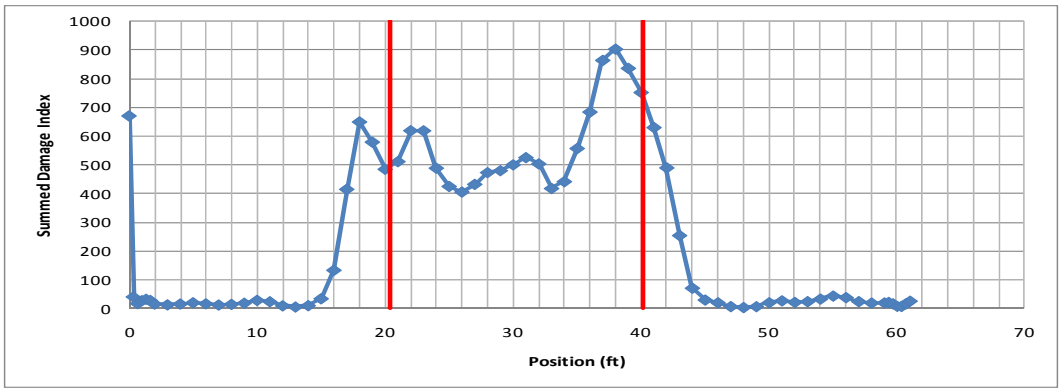

Figure 4.29 Summed damage index for beam 1

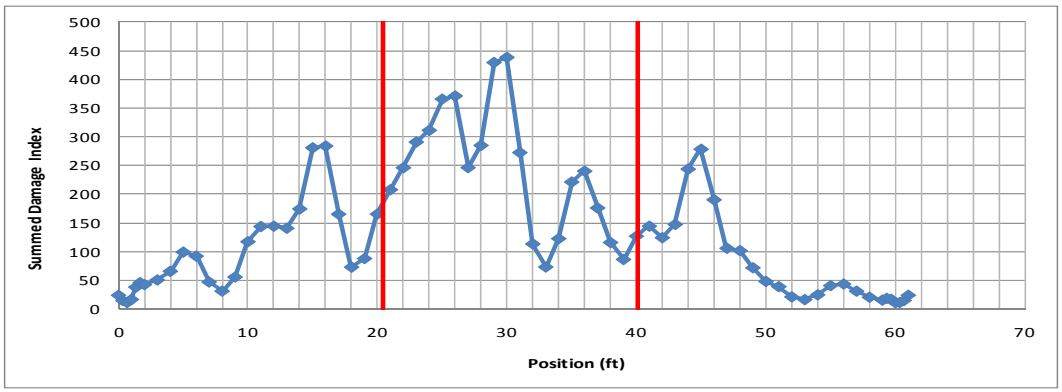

Figure 4.30 Summed damage index for beam 2

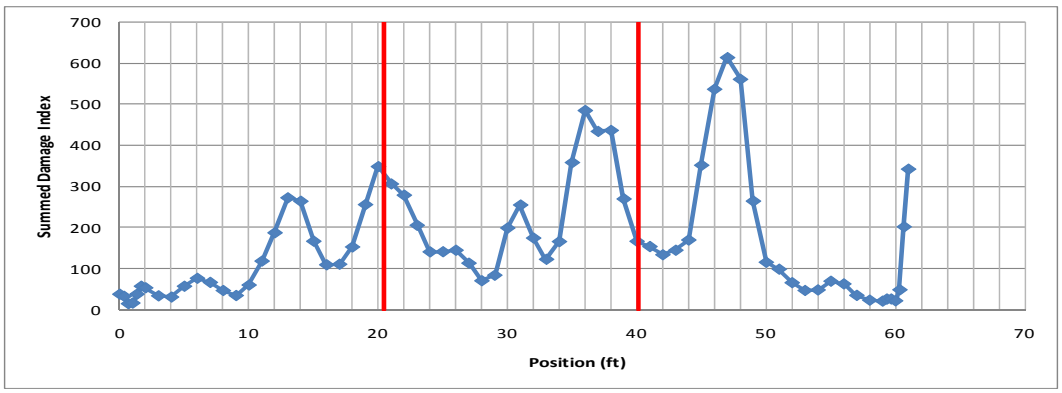

Figure 4.31 Summed Damage index for beam 3

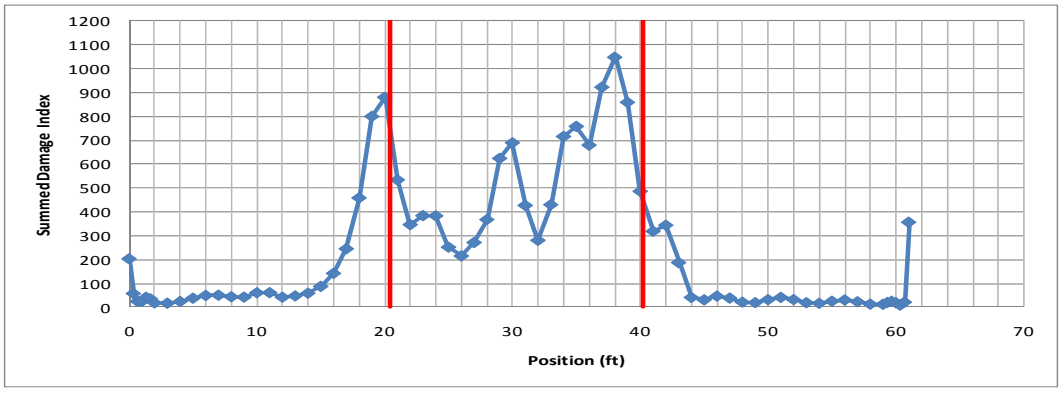

Figure 4.32 Summed damage index for beam 4

The summed damage indices presented above seem to accurately indicate the behavior of the beams in a very global sense (i.e., the presence of a highly stiffened middle region was detected). If extreme damage was present on the beams, it may be evident from these plots;

however, it is unlikely that small to moderate levels of damage can be detected using operational data with the curvature method and GSM.

4.3.2.3 Diaphragm Members

Figures 4.33-4.36 show summed damage indices for diaphragm rows 1-4, respectively. The dashed black lines indicate the location of interior beams. Therefore, each plot actually shows the summed damage index of three independent channel sections. The summed damage indices do not seem to indicate any discernable regions of changed dynamic characteristics for the four diaphragm rows. Because the diaphragm members are often much larger sections than necessary (C15x33.9 is the DOT minimum required section), it is unlikely that damage would be present in these members. If damage were present in the diaphragm members, it is not evident whether or not the ODSFRF curvature method would be capable of detecting and locating it.

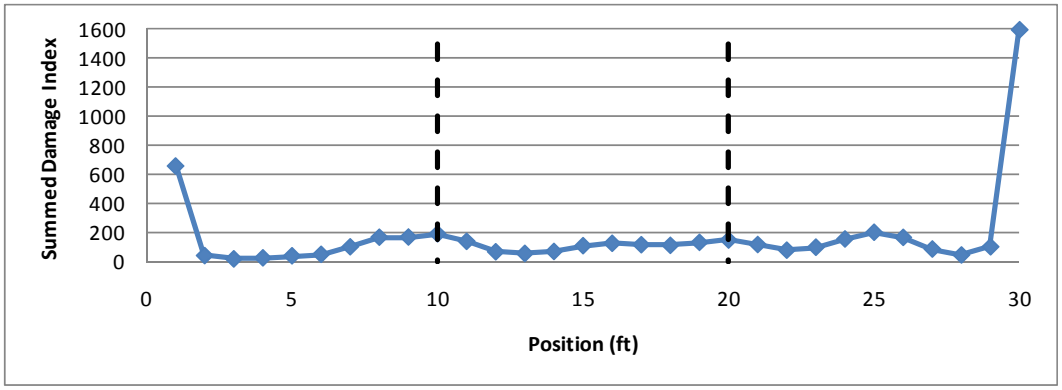

Figure 4.33 Summed Damage index for diaphragm row 1

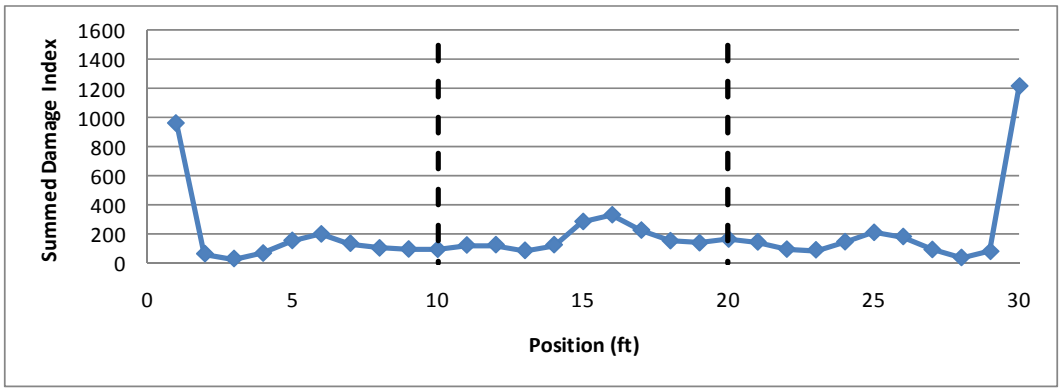

Figure 4.34 Summed damage index for diaphragm row 2

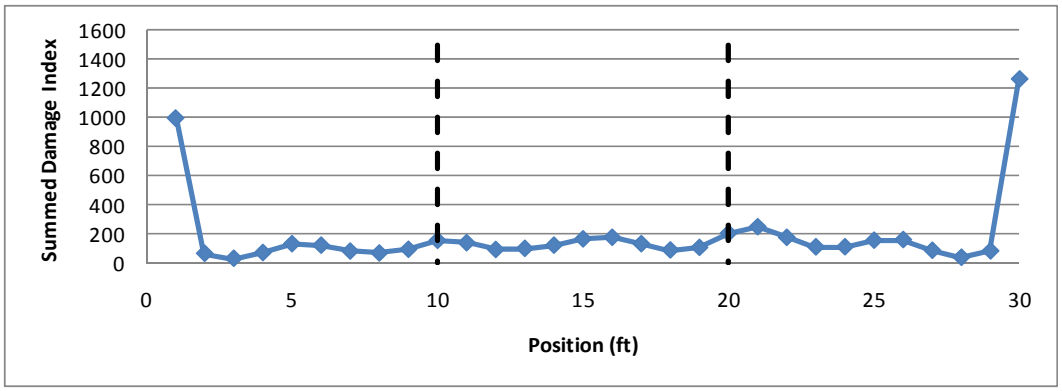

Figure 4.35 Summed damage index for diaphragm row 3

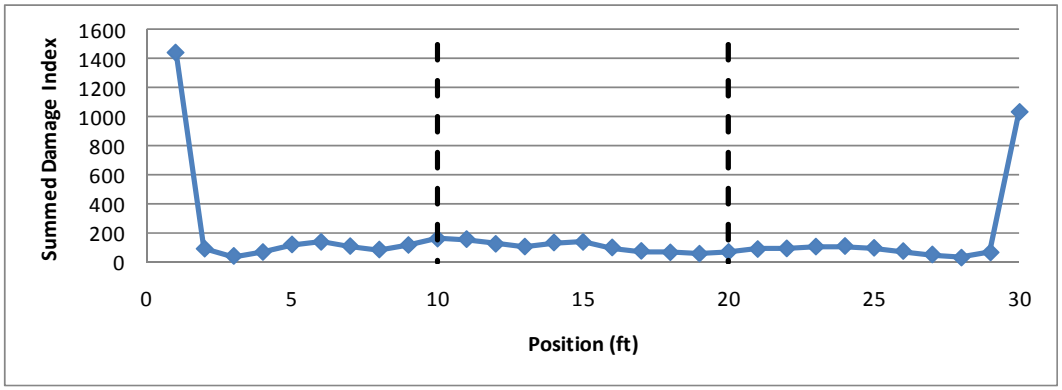

Figure 4.36 Summed damage index for diaphragm row 4

4.3.2.4 Analysis of Real Motion of Structure

By assigning the 440 ODSFRFs in Figure 4.28 to their actual measurement points as shown in Figure 4.24, the actual motion of each point of the structure relative to the reference response at the midpoint of the third beam can be calculated and animated using MEscope software. This allows users to visualize the effect of an average automobile traversing the bridge. Figure 4.37 shows a screenshot of the animation of the ODSFRFs at 13.5 Hz, which causes the intermediate diaphragm members to have first mode bending (*see Electronic Appendix video #1 for animation*). Although the animation of the girders seems to be too noisy to indicate a clear bending pattern, the motion of the diaphragm members dictates that the beams must be experiencing bending similar to the first mode shape. To verify this hypothesis, the FRF results from independent beam tests (Section 4.3.1) were animated at a frequency of 13.5 Hz. As shown in the screenshot in Figure 4.38, the beams experience first

mode bending at 13.5 Hz when measured independently (*see Electronic Appendix video #2 for animation*). The first bending mode of the structure at 13.5 Hz could be responsible for lateral cracks in the bottom of the concrete deck. Figure 4.39 shows a lateral crack in the concrete deck near the midspan of the bridge.

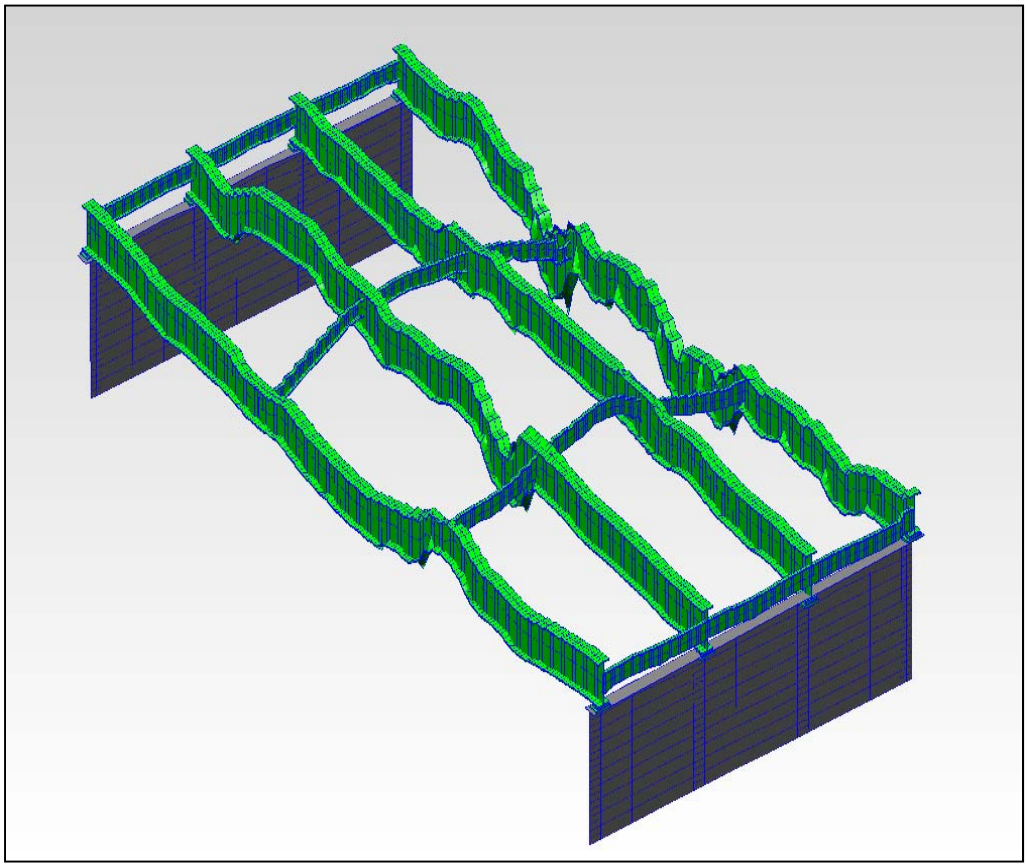

Figure 4.37 Screenshot of MEscope animation of entire bridge ODSFRFs at 13.5 Hz

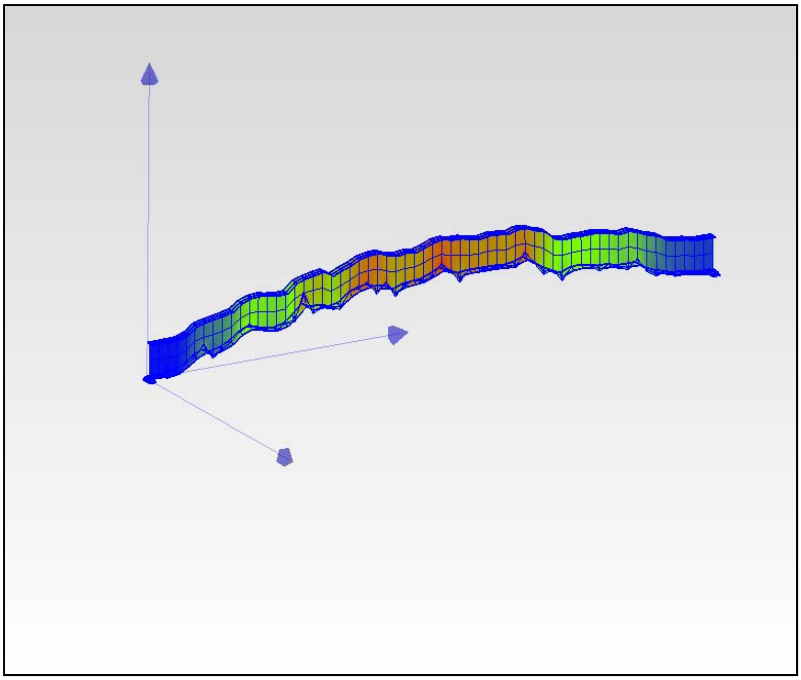

Figure 4.38 Screenshot of MEscope animation of independent beam FRFs at 13.5 Hz

Figure 4.39 Lateral surface crack in concrete deck near midspan of bridge

Furthermore, the first bending mode of the diaphragm members must cause torsion in the exterior beams, assuming the bolt connections are rigid. Although the animation of the structure shows that the end diaphragm members move significantly less than the

intermediate diaphragm rows, the abutment seat is being subjected to back-and-forth torsional motion from each beam, as shown in Figure 4.40. Figure 4.41 shows a schematic of the motion zoomed in at a single exterior beam.

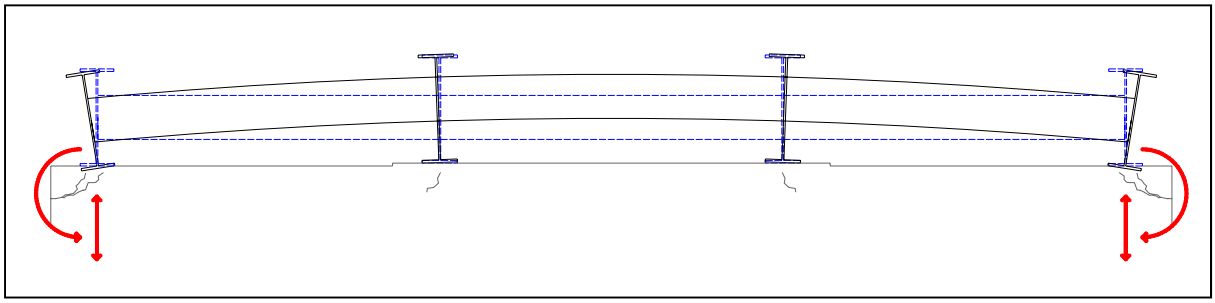

Figure 4.40 Schematic of torsional and compression-tension action caused by first bending mode of diaphragm members

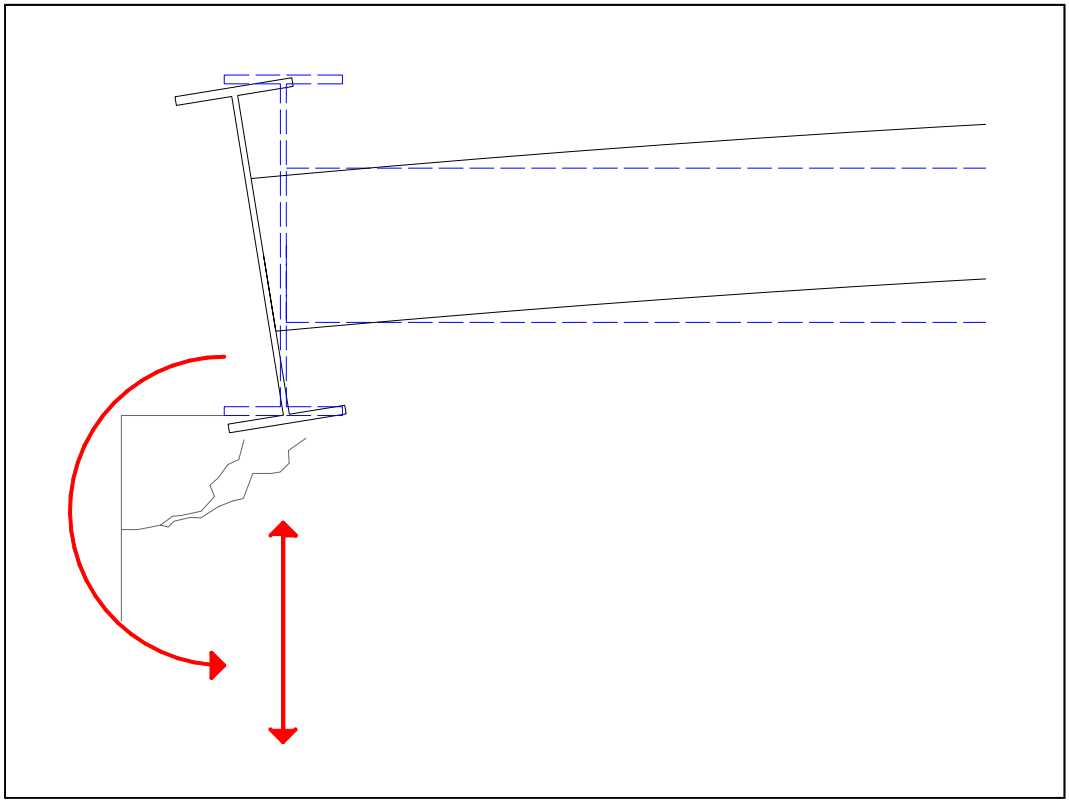

Figure 4.41 Zoomed-in schematic of torsional and compression-tension action caused by first bending mode of diaphragm members

Figure 4.42 shows a screenshot of the animation of the ODSFRFs at 15 Hz and is focused around the northeast boundary condition of beam 4 (*see Electronic Appendix video #3 for*

animation). It is clear that the abutment wall is experiencing cyclic tensile-compressive loading due to the motion of the beam and end plate assembly. Certain frequencies including 13.5 Hz and 19.5 Hz cause this type of motion in some or all of the abutment spots measured, however response was greatest beneath the exterior beams. This tensile-compressive action identified with ODS animations could play a role in the significant deterioration of concrete seen around the exterior beams. Figure 4.43 shows a large crack in the abutment wall near the north east boundary condition of beam 4, propagating from the bearing plates.

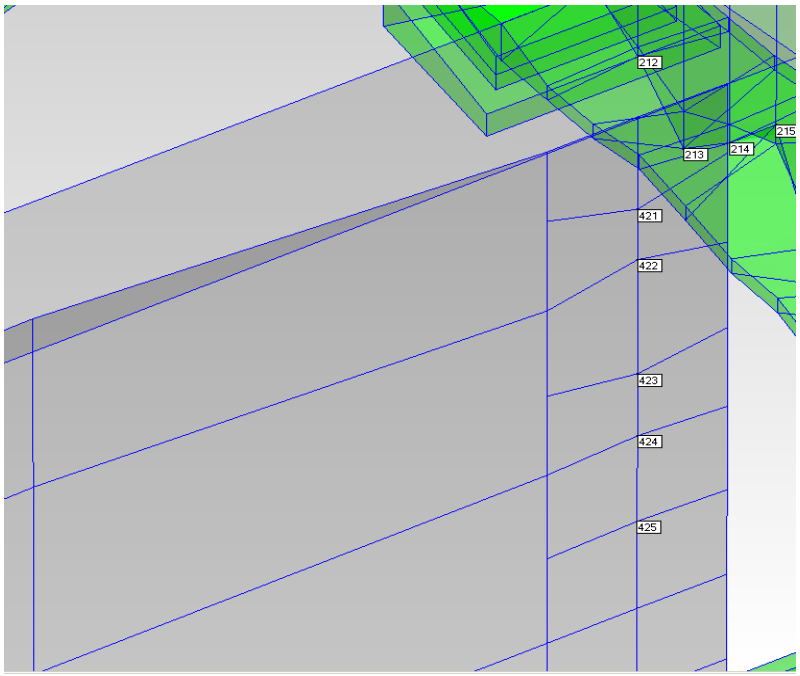

Figure 4.42 Screenshot of MEscope NE4 boundary condition animation of ODSFRFs at 15 Hz

Figure 4.43 Large crack in the northeast abutment wall beneath beam 4

4.3.3 Independent Forced Vibration End Beam Test

The third test that was run was a forced vibration test that focused on the boundary conditions of the beams. Two end plate assemblies were chosen for analysis: northeast support of beam 3 and northeast support of beam 4. A fine mesh of response points was used that included accelerometers on the bottom flange on either side of the web and the bearing plates supporting the beam. Also, the concrete seat in front of the boundary condition of beam 3 was measured. A point ten feet from the end of each beam was chosen as the excitation point and was impacted in the vertical direction. Figure 4.44 shows a 3-D rendering of a typical beam end with 42 labeled points (30 on the beam flange, 6 on the lowest bearing pad, and 6 on the concrete seat). Beam 4 had noticeable deterioration of the bottom flange near the boundary condition, and the same area on beam 3 was relatively clean, as shown in Figures 4.45 and 4.46.

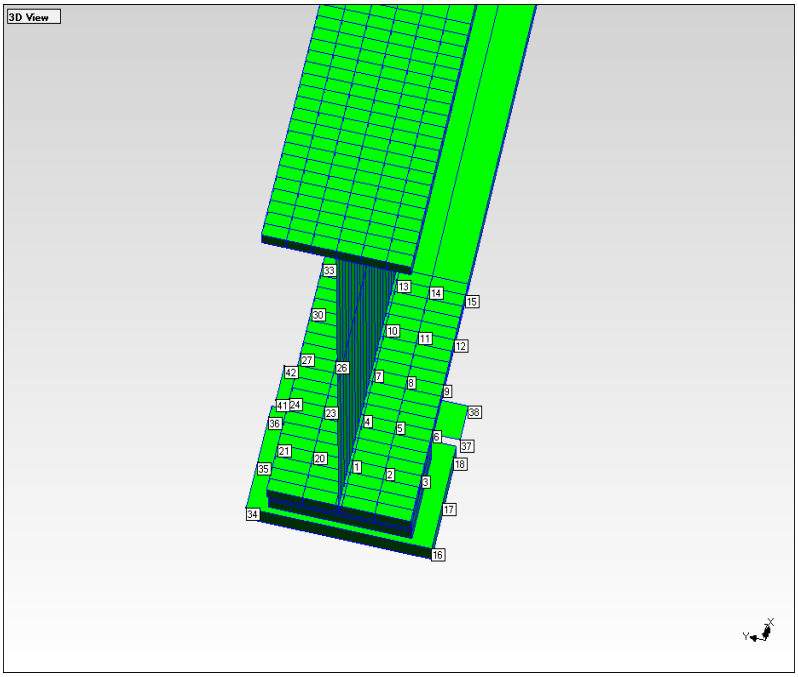

Figure 4.44 Rendering of a typical beam end and boundary condition with 42 response points

Figure 4.45 Forced vibration response measurement of northeast end and boundary condition of beam 3

Figure 4.46 Forced vibration response measurement of northeast end and boundary condition of beam 4 with noticeable deterioration of the bottom flange

4.3.3.1 Analysis of Relative Motion of Beam End

Figures 4.47 and 4.48 show overlaid FRFs from 0-125 Hz. They were calculated from data gathered in two independent forced vibration tests on the northeast boundary condition/end of beam 4 and the northeast boundary condition/end of beam 3, respectively. The FRFs look fairly noisy because response points were distributed across various substructures of the end beam assembly, as shown in Figure 4.43. Because the response points crossed structural boundaries, these results were not used in damage detection algorithms, but instead were used to understand the relative motion between points caused by a forced excitation.

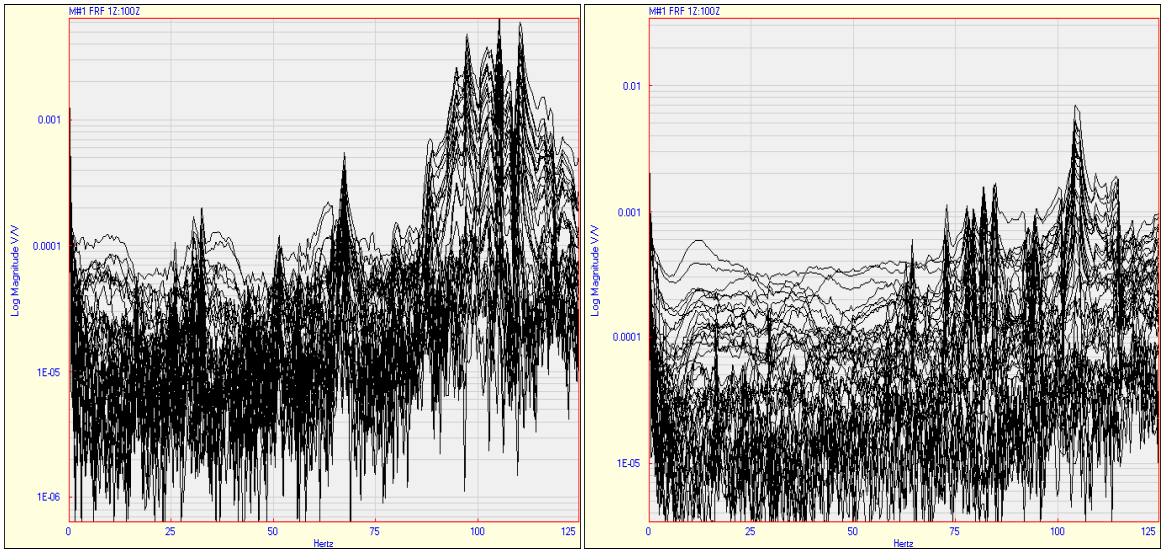

Figure 4.47 Overlaid FRFs from forced vibration test on northeast boundary condition and end of beam 4 and Figure 4.48 Overlaid FRF's from forced vibration test on northeast boundary condition and end of beam 3

By assigning the FRFs in Figures 4.47 and 4.48 to their actual measurement points as shown in Figures 4.45 and 4.46, the relative motion of each point of the structure due to a vertical impact can be calculated and animated using MEscope software. From these animations, it is possible to determine which frequency ranges cause significant motion of the bearing plates (*see Electronic Appendix videos #4 and 5 for animations*). Figure 4.49 shows a screenshot of the north east boundary condition of beam 3 animated at a high frequency (151 Hz), and Figure 4.50 shows the northeast boundary condition of beam 4 animated at a low frequency (1 Hz). Both screenshots seem to show that the bearing plates are moving with significant motion compared to the beam flange, which is expected to vibrate significantly from an

impact. It was found that intermediate frequencies (such as 43.5 Hz) cause very little motion in the plates relative to the beam flange, as shown in Figure 4.51 (*see Electronic Appendix video #6 for animation*).

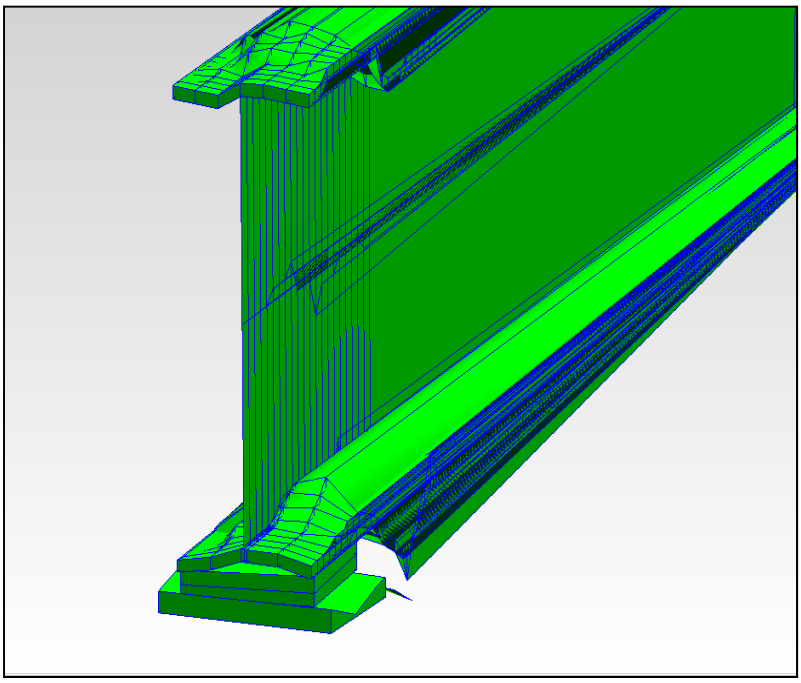

Figure 4.49 Screenshot of MEscope NE3 boundary condition animation of FRFs at 151 Hz

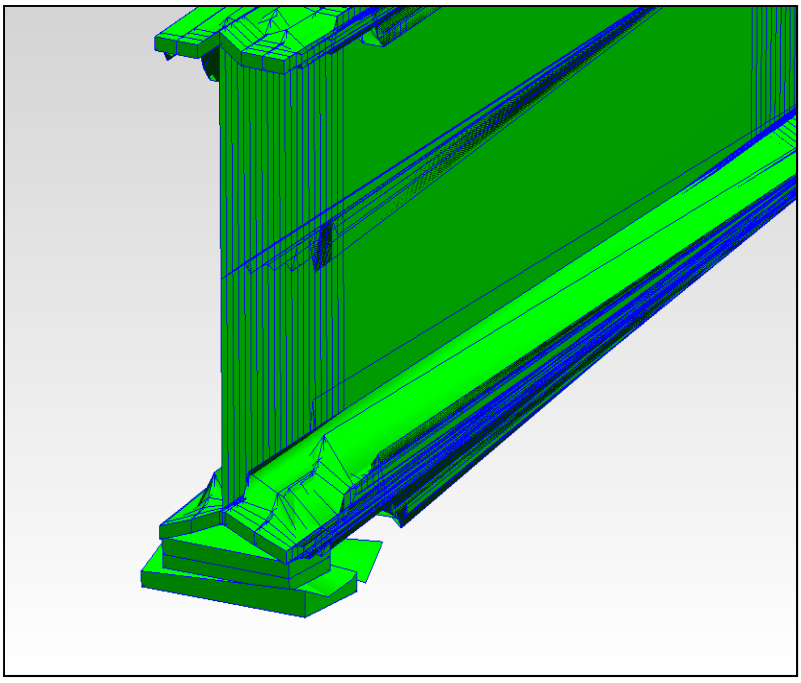

Figure 4.50 Screenshot of MEscope NE4 boundary condition animation of FRFs at 1 Hz

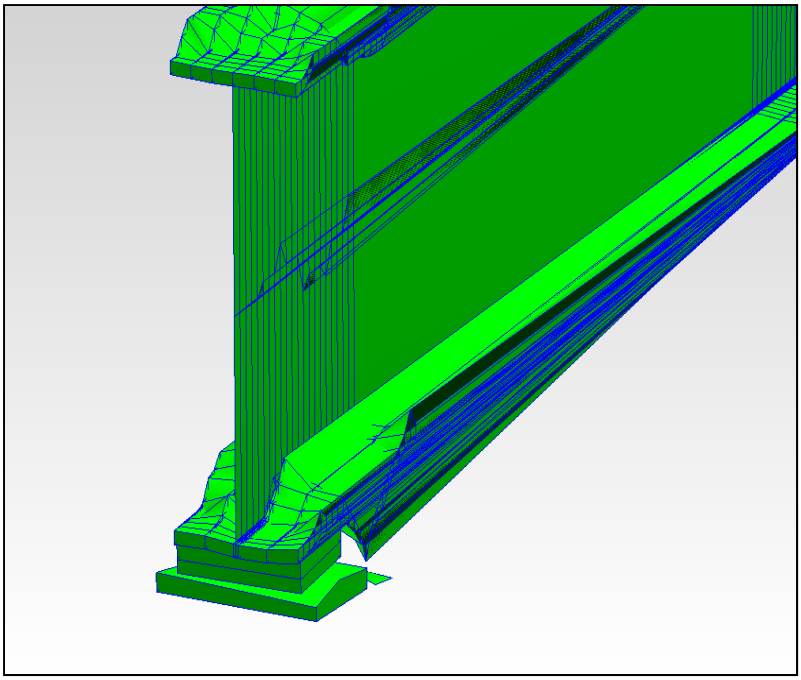

Figure 4.51 Screenshot of MEscope NE4 boundary condition animation of FRFs at 43.5 Hz

To further exemplify the torsional component of motion on the exterior beams, screenshots of the relative response of an exterior beam end (NE4) and interior beam end (NE3) are shown in Figures 4.52 and 4.53, respectively (*see Electronic Appendix video #7 and 8 for animations*). Both figures show the beams vibrating at 13.5 Hz, which is the first mode shape of the structure. As shown in Figure 4.52, the exterior beam end including the bearing plates twist significantly due to a vertical impact whereas Figure 4.53 shows almost no off-center motion in the interior beam end.

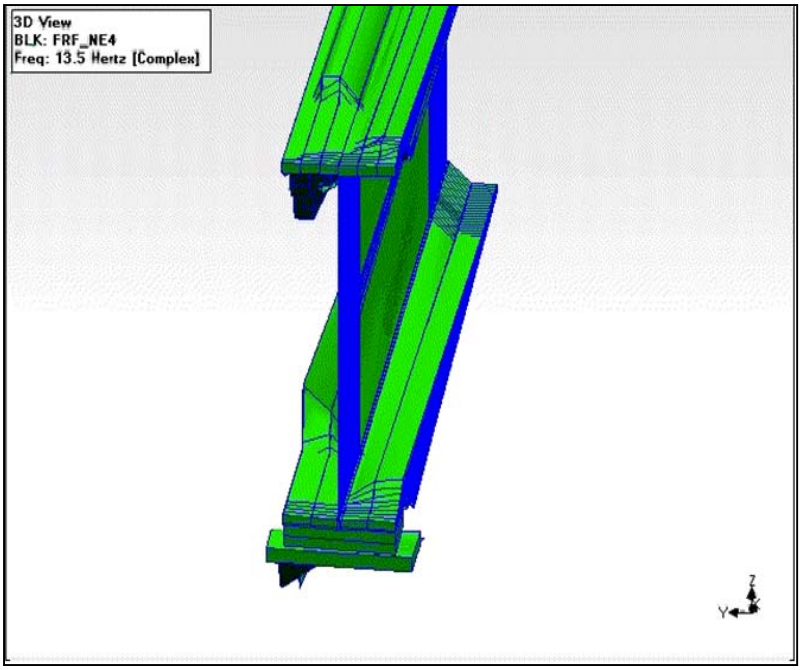

Figure 4.52 Screenshot of MEscope NE4 (exterior beam) boundary condition animation of FRF's at 13.5 Hz showing significant torsional motion

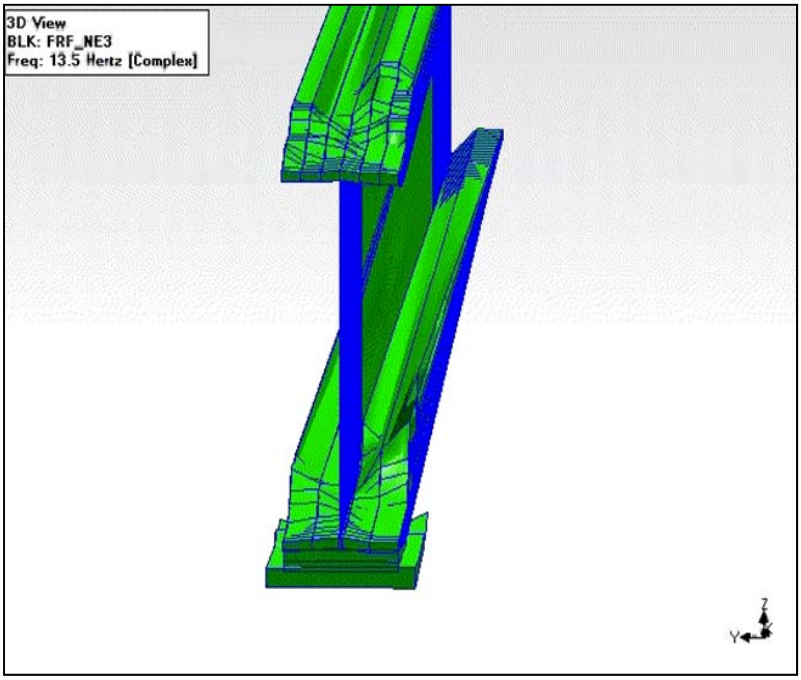

Figure 4.53 Screenshot of MEscope NE3 (interior beam) boundary condition animation of FRF's at 13.5 Hz showing very little torsional motion

4.3.4 Frequency-domain Analysis of Traffic

To determine the effect of traffic passing over the bridge, the response of the reference accelerometer from every recorded operational vibration data set was analyzed. Figure 4.54 shows overlaid time waveforms from 88 different automobiles. As shown, most time waveforms had peak acceleration magnitudes below 0.4 g, and significant vibration typically lasted for less than 1.5 seconds

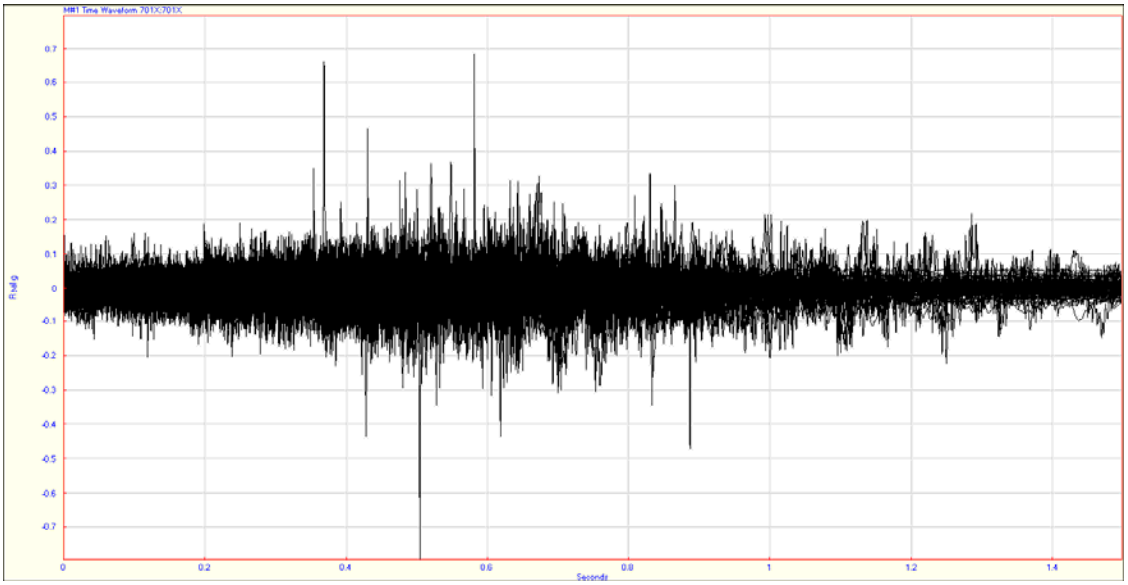

Figure 4.54 Overlaid time waveforms from 88 different automobiles

To analyze the frequency components of the average automobile, the Fourier transform of the 88 time waveforms from Figure 4.54 was calculated. Figure 4.55 shows the resulting overlaid frequency waveforms. As shown, there is significant frequency contribution of most, if not all data samples at approximately 13.5 Hz. The highest magnitude of the frequency waveform is also at 13.5 Hz. Therefore, the operational bending shape shown in Figure 4.37 can be considered a common occurrence for this particular structure and traffic load. Consequently, it can be assumed the damage correlated with this operational bending shape (shown in Figures 4.39 -4.43) will continue to occur if the frequency components of the traffic load or frequency response function of the structure are not altered.

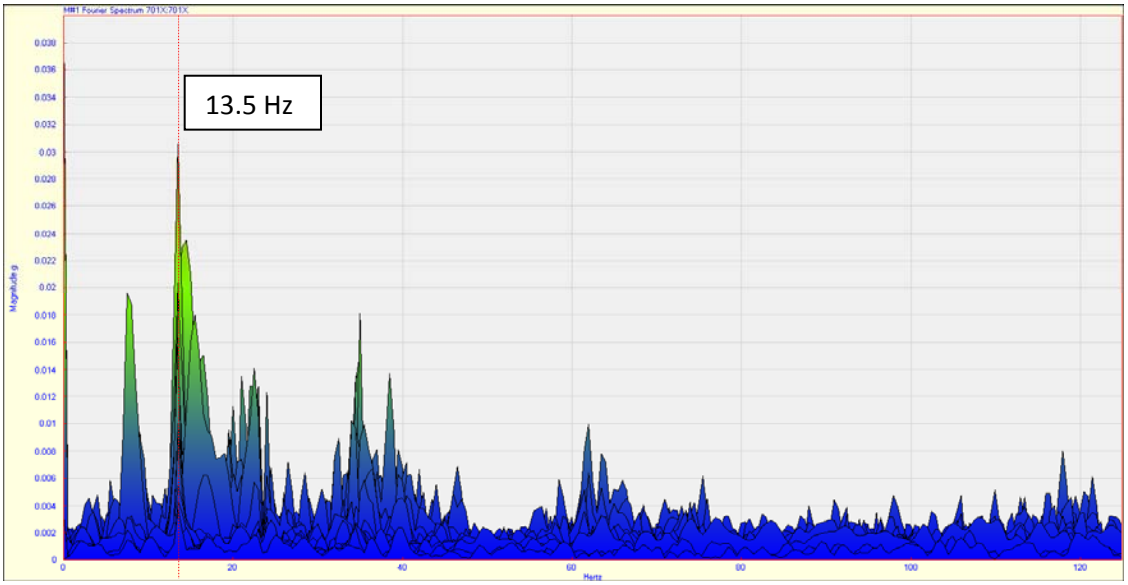

Figure 4.55 Overlaid frequency waveforms from 88 different automobiles

5. CONCLUSION AND RECCOMENDATIONS

Vibration-based damage identification (VBDI) techniques were studied to assess their applicability to DOT highway bridges. These techniques, namely the FRF curvature method with various fitting parameters, were used in numerical simulations, laboratory experiments, and field experiments.

Numerical simulations on a plate with two damage locations of varying severity showed that the FRF curvature method is theoretically capable of locating and quantifying damage with great accuracy using either local or global curve fitting. When noise was introduced, the accuracy and precision of damage identification was dependent on damage severity. A large change in cross section (60%) was identified with 1% added random noise, but a small change in cross section (5%) was not detected. Numerical simulations are useful in that they show the significant impact of noise on various damage detection algorithms. Because all vibration-based experiments introduce noise from various sources (transducers, environment, etc.), it is important not only to limit this noise but to understand its inevitable effect on damage detection.

Laboratory experiments were first completed on an I-beam. This structure was relatively simple; its cross section was highly uniform and its boundary conditions were simplistic. To simulate damage in the laboratory, masses were fixed to the top flange of the structure. In the first experiment, a small mass (1.8% of total beam mass) and a large mass (6% of total beam mass) were accurately located with high precision using the FRF curvature method with local curve fitting. However, this method was unable to quantify the damage correctly, showing a greater change in curvature around the small mass than large mass. This is most likely due to the location of the small mass, which was toward the middle of the beam, where there is maximum deflection. Further investigations could focus on the effect of location on damage quantification, with equivalent single-mass tests at various locations across the structure. A segmented approach could be developed to analyze portions of a structure separately from each other.

A new approach to curve fitting was considered using the same data from the two-mass test. This approach first used global curve fitting and then locally curve fit the data to create a

synthetic baseline structure. Both mass locations were accurately identified and quantified (the large mass showed a much larger change in curvature than the small mass). Although this double-fitting method shows promise, it is highly dependent on the parameters chosen during global fitting, and more experiments need to be run to test its applicability to real structures.

Using the same two-mass setup, a nodal mesh study was conducted to determine the effect of excitation distance on damage detection results from a roving excitation test. Three experiments were run using excitation spacing of 2 inches (2.5% of total beam length), 4 inches (5% of total beam length), and 6 inches (7.5% of total beam length). Only the test using excitation spacing of 2 inches (in addition to the standard 1 inch spacing test) was able to accurately locate the damage locations. This study provided the necessary knowledge to determine nodal spacing for the scale bridge and field experiments.

The final test run on the I-beam was a single damage location test with clamps fixed to the outer edge of the top flange. These clamps represented 3.7% of the beam's total mass. Similar to the two-mass test, the FRF curvature method with local curve fitting was able to correctly locate the presence of the clamps. This study showed that a roving excitation test on the centerline of the I-beam was independent of whether or not the damage was also located on the centerline.

Laboratory testing was also completed on a 1/6 scale model of a single span, steel girder highway bridge. A forced excitation, roving response test was run on the baseline structure to see if the diaphragm members could be located as highly stiffened regions. The FRF curvature method with local curve fitting was able to clearly locate a stiffened region in the middle two-thirds of the bridge. Therefore, the effect of the diaphragm members in this sort of a structure is more spread out than the assumed local region surrounding each diaphragm member. This same test was then run with a mass (3.2% of total structure mass) fixed to the top flange of one of the beams. The FRF curvature method with local curve fitting showed that the beam without the mass had virtually the same behavior as the baseline test. The beam with the mass had a much different damage index that no longer showed the highly stiffened region between the intermediate diaphragm members. However, the damage detection algorithm was unable to locate the mass. Further testing could increase the size of

the mass until it was located using this method and also increase the density of the response mesh on the beams.

An operational vibration test was simulated on the scale bridge by impacting multiple points on the top flanges of each beam and averaging all responses. The actual motion of each response point was then animated. Various operating shapes were identified, and the bending characteristics of the diaphragm members in relation to the girders were recognized. Hypotheses were made regarding frequencies that would cause significant damage if a deck and abutment were present. Further work could focus on expanding this structure to resemble a bridge more closely, with a wood or concrete deck and some sort of external abutment. The same operational response testing could then be completed and analyzed to correlate actual motion with damage in the laboratory.

Early field experiments were completed on a single-span composite steel girder, concrete deck bridge. The first test run attempted to acquire data for all four girders during a roving response test with a single fixed excitation point on an exterior beam. Accelerometers were roved with the help of a DOT Snooper truck that was parked on the bridge during the excitation. The FRF curvature method with local curve fitting was used to create damage indices for each beam; however, only the beam with the impact yielded usable data. The damage index for this beam (beam 4) clearly showed the impact location and small areas of stiffness around each intermediate diaphragm member. The other three damage indices were too noisy to make any conclusions because the impact excitation was so heavily damped by the time it reached other members.

Later field experiments were completed on the same DOT bridge but without the Snooper truck. Instead, scaffolding was used to reach the entire superstructure. Because earlier testing showed that excitation on a single beam was not adequate for detecting damage on the entire structure, the first test that was run was an independent roving response test for each beam. This test yielded the highest quality FRFs for any test run on the field bridge. Using the FRF curvature method with local curve fitting, four separate damage indices were created. All four showed the impact point, but the stiffened regions around the diaphragm members were only located on the exterior beams. Other changes in FRF curvature were too

random and spread out to signify the presence of a change in dynamic properties due to damage.

The most extensive test run on the DOT bridge was a global operational vibration test with response points on the beams, diaphragm members, and abutment wall. This test used vibration caused by traffic as an unknown excitation and a reference accelerometer as the input; likewise, roving accelerometers were the output. The ODSFRF curvature method was used to create damage indices for the four beams and four rows of diaphragm members. The damage indices for the exterior beam very clearly showed a highly stiffened region between the intermediate diaphragm members. The damage indices for the interior beams indicated the same stiffened region between the diaphragm members but also extended out well past these locations. This larger stiffened region, covering approximately two-thirds of each interior beam, is very similar to the characteristics seen in the laboratory scale bridge. Damage indices for the diaphragm members showed no discernable changes in FRF curvature, meaning that all locations measured had very similar levels of stiffness and damping.

The most influential use of data collected on the field bridge was through an analysis of operational motion by animating actual response data. All 440 response points measured during the global operational vibration test were animated using an average automobile frequency response function (by overlaying 88 ODSFRFs). The first mode shape of the diaphragm members and beams was determined to be 13.5 Hz. The motion of the bridge as a whole was animated at this frequency and correlated with noticeable lateral cracking in the concrete deck near the intermediate diaphragm rows. Also, frequencies causing torsional and compression-tension action experienced by the abutment directly beneath the exterior beams were correlated with both significant and minor cracking in those regions of the abutment. The frequencies that caused the most significant torsional and compression-tension action were between 12-20 Hz. Similarly, an analysis of relative motion of two bearing plates and beams ends was completed. It was found that high and very low frequencies cause the beam end and bearing plate assembly to vibrate with significant motion relative to the beam flange. Intermediate frequencies between 15 Hz and 100 Hz were found to cause very little motion in the end plates.

To understand the frequency components of the traffic load relative to the reference accelerometer during the operational vibration test, the time waveforms of all 88 automobiles used in the test were converted to the frequency domain. By overlaying all frequency waveforms, it was found that the traffic load contributes most to a frequency of 13.5 Hz, which is to be expected (13.5 Hz is the fundamental frequency of the bridge). However, virtually every automobile signal had large frequency content not only at 13.5 Hz but at 9.5 Hz and from 13.5-15 Hz. These observations are important in that the response of the structure can be viewed at any of these "common" frequencies and compared with "problem" frequencies (those that cause motion detrimental to the structure).

Field testing with both forced and operational excitation was not able to identify any localized information about the structure. Global characteristics such as stiffened regions due to the presence of lateral diaphragm members were adequately located in some cases, but this does little in the way of improving the life of structure. Furthermore, if and when VBDI becomes a powerful tool in detecting damage in real civil infrastructure, it has no way of correlating this damage with a cause or providing a solution to the problem. Analysis of the operational response of the structure may provide an effective way of recognizing global trends in bridge response, correlating motion with damage, and comparing excitation frequencies with problem frequencies. Current damage detection methods (i.e., visual inspection, tap test, etc.) can be used right now with operational response analysis to begin recognizing the root causes of various damage types. In the future, advanced damage detection techniques (VBDI, imaging, etc.) can be used to supplement the operational response analysis and provide an even broader base for correlating damage with causes. While the field of traditional vibration-based damage identification continues to mature, further work should (1) perfect the process of collecting high-quality operational frequency response data; (2) expand and simplify the process of correlating frequency response animations with damage; and (3) develop efficient, economical, pre-emptive solutions to common damage types.

REFERENCES

Adewuyi, A. P., Wu, Z., & Serker, N. K. (2009). Assessment of Vibration-based Damage Identification Methods Using Displacement and Distributed Strain Measurement. *Structural Health Monitoring , 8*, 443.

Chang, P. C., Flatau, A., & S.C., L. (2003). Review Paper: Health Monitoring of Civil Infrastructure. *Structural Health Monitoring , 2*, 257.

Farrar, C., & Jauregui, D. (1994). *Damage Detection Algorithms Applied to Experimental and Numerical Modal Data from the I-40 Bridge.* Technical Report, Los Alamos National Laboratory, N.M.

Guo, G. Q., Xiaozhai, Q., Dong, W., & Chang, P. (2005). Local Measurement for Structural Health Monitoring. *Earthquake Engineering and Engineering Vibration , 4* (1), 165-172.

Iowa Department of Transportation. (n.d.). *Primary Structures.* Retrieved April 2010, from Bridges in Iowa: http://www.iowadot.gov/pdf_files/Primary_Structures.pdf

Li, S., & Wu, Z. (2007). A Non-baseline Algorithm for Damage Locating in Flexural Structures Using Dynamic Distributed Macro-strain Responses. *36*, 1109-1125.

Liu, X., Lieven, N., & Escamilla-Ambrisio, P. (2009). Frequency Response Function Shape-based Methods for Structural Damage Localization. *Mechanical Systems and Signal Processing , 23*, 1243-1259.

Maia, N., & Silva, J. A. (2003). Damage Detection in Structures: from Mode Shape to Frequency Response Function Methods. *Mechanical Ssystem Signal Processing , 17* (3), 489-498.

McHargue, P., & Richardson, M. (1993). Operating Deflection Shapes From Time Versus Frequency Domain Mesaurements. *11th IMAC Conference.* Kissimmee.

Pandey, A., Biswas, M., & Samman, M. (1991). Damage Detection from Changes in Curvature Mode Shapes. *Journal of Sounds and Vibration , 145* (2), 321-332.

Ratcilffe, C., Crane, R., & Gillespie, J. (2004). Damage Detection in Large Composite Structures using Broadband Vibration Method. *Journal of the British Institute of Non-destructive Testing , 46* (1), 10-16.

Ratcliffe, C. P. (2009). Local Damage Detection with the Global Fitting Method Using Mode Shape Data in Notched Beams. *Journal of Nondestructive Evaluation , 28*, 63-74.

Richardson, M., & Formenti, D. (1985). Global Curve Fitting of Frequency Response Measurements using Rational Fraction Polynomial Method. *3rd IMAC Conference.* Orlando.

Roberts, G. W., Meng, X., & Dodson, A. H. (2004, May). Integrating a Global Positioning System and Accelerometers to Monitor Deflection of Bridges. *Journal of Surveying Engineering* , 65-72.

Rytter, A. (1993). *Vibration-based Inspection of Civil Engineering Structures.* PhD Thesis, Alborg University, Dept of Building Technology and Structural Engineering.

Sampaio, R. M., & Silva, J. (1999). Damage Detection Using the Frequency-Response-Function Curvature Method. *Journal of Sound and Vibration , 226* (5), 1029-1042.

Schwarz, B., & Richardson, M. (2004). Measurements Required for Displaying Operating Deflection Shapes. *22nd IMAC Conference.* Dearborn.

U.S. Department of Transportation Federal Highway Administration. (2010, February 5). *FHWA Bridge Programs Structure Type by Year Built.* Retrieved April 2010, from Structures: http://www.fhwa.dot.gov/bridge/nbi/yrblt09.cfm

Zhao-Dont, X., & Zhisen, W. (2007). Engery Damage Detection Strategy Based on Accerleration Responses for Long-span Bridge Structures. *Engineering Structures , 29*, 609-617.